國立臺灣大學理學院大氣科學研究所

碩士論文

Graduate Institute of Atmospheric Sciences

College of Science

National Taiwan University

Master Thesis

利用氣膠模式探討環境腔 α-蒎烯臭氧化反應的粒子核化

A Model Study of New Particle Formation from α-pinene
Ozonolysis in the Environmental Chamber Using MOSAIC

朱清緯

Ching-Wei Chu

指導教授：洪惠敏　博士

Advisor：Hui-Ming Hung, Ph.D.

中華民國 109 年 7 月

July 2020

國立臺灣大學碩士學位論文
口試委員會審定書

　　本論文係 朱清緯 君（學號 R07229011）在國立臺灣大學大氣科學學系、所完成之碩士學位論文，於民國 109 年 7 月 22 日承下列考試委員審查通過及口試及格，特此證明

口試委員：

洪惠敏 （簽名）

（指導教授）

陳維婷　　　　　_陳正平_

系主任、所長　_林博雄_　　（簽名）

致謝

在這不長不短的兩年碩士生涯，若沒有諸位師長及友人一路上的協助與鼓勵，是沒辦法在這裡寫致謝的。首先要感謝我的指導教授－洪惠敏老師，自大學時期便帶領我踏入大氣化學這有趣的領域，也引起了對此的興趣，因而來到大氣化學實驗室的門口前(即使當初熟悉的門口已經被收到系上儲藏室了)。由衷感謝老師在這段期間細心地傳授知識及耐心地督促指導，也願意讓我在研究的藍圖上自由發揮，並從旁給予寶貴的建議與指正。同時也謝謝老師在過程中的包容與關心，讓我能以最好的狀態去面對研究上的挑戰。此外也相當感謝口試委員－陳正平老師，在 group meeting 中能精準點出研究裡不足或有誤的地方並給出有力的建議，讓此論文得以更加嚴謹。另外也非常感謝口試委員－陳維婷老師，在口試期間提供許多學術撰寫上的建議，使得此論文更加通順。最後感謝三位老師撥冗審閱此份論文，在此致上最高的謝意！

在進入研究所前，感謝浩維及任廷兩位學長的帶領與協助，特別要感謝浩維在實驗上詳細地指導每個該注意的環節，讓本研究的實驗得以順利完成。除此之外，非常感謝實驗室好夥伴亭羽在研究與課業上相互勉勵以及共同打理實驗室的一切，同時也幫助身為外系的我快速融入大氣系這個環境，也讓這條研究路上走得相當順遂且歡樂。接著要感謝幾乎是住在實驗室的維傑，這段期間給予相當多的協助，並在實驗室維護上幫了不少忙，也從中學到不少領域外知識。另外也感謝佳莉學姐一同架起工作站系統與模式測試，讓實驗室有了更多研究工具與可能性。感謝奕翰和佳暄為實驗室帶來更多歡笑以及食物，也謝謝陸陸續續進來的成員們品潔、毓琇、定洋。感謝工作站上的哥吉拉(2019)在我模式面臨到 debug 輪迴之時，當天把你擺上主機上後晚上就解決了最致命的 bug，讓我順利完成研究。在此非常感謝實驗室

i

的各位，在嚴峻的研究路上給予我繼續前進的動力之餘也帶給我碩士生涯許多愉快的回憶！

感謝 Melody Hsieh 的陪伴與鼓勵及好友們在這一路上的支持與打氣，在為論文奮鬥過程中能夠感受到滿滿溫暖。謝謝家裡提供經濟支援，在求學過程中無後顧之憂。此外也謝謝室友牡丹鸚鵡，在我獨自看著螢幕敲著鍵盤之時不忘叫個幾聲討顆種子，讓我知道不是只有我一人在奮鬥。最後，僅將這份完成碩士學位的喜悅分享給所有幫助及鼓勵我的你們，感謝你們！

Acknowledgments

中文摘要

　　由 α-蒎烯臭氧化反應衍生出的新生粒子事件即使在實驗室及實地的研究中可被觀測到，但是目前大多的空氣品質模式卻缺乏對這類純有機物核化的描述，而其很有可能是一個重要的新生粒子來源。於是本研究利用氣膠模式(MOSAIC)及古典核化理論來模擬哈佛環境腔(HEC)以及流動管反應器(FTR)下的 α-蒎烯臭氧化反應的新生粒子事件，當中分別使用 175 bin 及 145bin 的粒徑分佈來進行模擬。在MOSAIC 中為了簡化臭氧化反應使用了雙產物模式，兩種產物分別為低揮發性有機物(LVOC)及半揮發性有機物(SVOC)，兩者皆可以參與凝結過程但其中只有LVOC 會主導核化過程。在靈敏度測試當中，不僅核化曲線可以影響新生粒子事件的強度，凝結相關參數也可以間接影響之，特別是粒子相擴散度對其可以有非線性的變化，而此表現可能來自其對粒子成長的限制作用。在模式中給予 α-蒎烯濃度一波動函數可以重現 HEC 中離散的新生粒子事件，也因此可推論這樣的浮動來自反應腔體內物種濃度的空間不均勻性。根據粒徑分佈的誤差分析後可以發現，在古典核化速率的表面張力為 23.0 dyne cm^{-1}、LVOC 及 SVOC 的調節係數分別為 0.1及 0.3 和 10^{-12} cm^2 s^{-1} 的粒子相擴散度可以適當模擬 HEC 實驗的粒徑分佈，但在眾數粒徑附近會有低估粒子數的狀況。另外，同樣的模式也被用來模擬 FTR 的反應，然而即使考慮到各種不確定的因素卻無法模擬出其粒徑分佈，推測此結果應該是兩個實驗反應的限量試劑及時間不同而使得生成物產率比值不同所致。

關鍵字：臭氧化反應、α-蒎烯、核化、粒子成長

Abstract
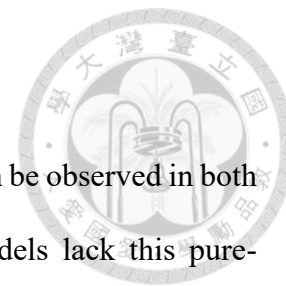
The new particle formation (NPF) from α-pinene ozonolysis can be observed in both field and laboratory studies. However, the current air quality models lack this pure-organic NPF, which might be an essential source of new particles. Therefore, the NPF of α-pinene ozonolysis in a continuously mixed flow reactor (Harvard Environmental Chamber, HEC) and a flow tube reactor were simulated respectively using 175-bin and 145-bin aerosol model, Model for Simulating Aerosol Interactions and Chemistry (MOSAIC) incorporated with classical nucleation theory (CNT). In this study, the α-pinene ozonolysis was expressed using a two-products model with low- and semi-volatile organic compounds (LVOC and SVOC) for simplification. The nucleation process was assumed to be dominated by LVOC while the condensation processes were contributed by both LVOC and SVOC. The sensitivity tests showed that not only the CNT nucleation curve but also the parameters of the condensation process can alter the strength of NPF. Especially for bulk diffusivity, the nonlinear response of NPF to that is likely due to the limited particle growth. Moreover, the spatial inhomogeneity in HEC, which took account for the discrete NPF was illustrated by the simulation with fluctuated α-pinene concentration. Based on the error analysis, the model with CNT surface tension of 23.0 dyne cm^{-1}, accommodation coefficients of 0.1 and 0.3 for LVOC and SVOC, and bulk diffusivity of 10^{-12} cm^2 s^{-1} gave a good performance in simulating the HEC experiments. However, it still underestimated the number density of particles with around mode size. The same model was also introduced to simulate the FTR experiments, and yet, failed to interpret the NPF regardless of considering the uncertainty. The inconsistency might result from the various LVOC to SVOC yield ratio, which carried out from different reactant-limiting ozonolysis between HEC and FTR experiments and reaction time.

Keywords: ozonolysis, α-pinene, nucleation, particle growth

Contents

List of Tables

List of Figures

Chapter 1　Introduction

1.1　Paper Review

1.1.1　Impacts of Aerosol on Environment

Atmospheric aerosol can affect the climate by aerosol-radiation and aerosol-cloud interaction, so-called aerosol direct (including semi-direct) and indirect effect, respectively. For direct effect, aerosol can directly change the direction of radiation propagation and intensity by scattering and absorption. These processes depend on the size of particles that can be estimated using the Mie theory. On the other hand, indirect effect means that aerosol acts as a cloud condensation nuclei (CCN) which can influence the droplet size, structure, and lifetime of clouds and further alter the cloud albedo. For instance, by increasing aerosol (or CCN) number density, clouds with smaller droplet sizes are formed which have a higher albedo (Twomey, 1977) and lifetime (Albrecht, 1989). This effect is the so-called first aerosol indirect effect or cloud albedo effect. The alteration of atmospheric energy budget by aerosol direct and indirect effects imposes radiative forcing to the climate system. The overall radiative forcing of both aerosol effects has been reported to be negative (cooling effect) according to the IPCC AR5 report (Stocker et al., 2013).

Furthermore, the impacts of aerosol on living beings are not negligible. As an air pollutant, aerosol can be inhaled and deposited in the respiratory tract. The particulate matters with a diameter less than 10 μm (i.e., PM_{10}) are inhalable and potentially hazardous to health. The finer particles such as $PM_{2.5}$ can be even more toxic because they have a larger residence time in the respiratory system and can adsorb more chemicals due to higher specific surface areas (Pope III & Dockery, 2006). These particles can

1

further trigger cardiovascular, respiratory, and allergic diseases which lead to a higher mortality (Bernstein et al., 2004; Pöschl, 2005). Besides, particulate matters can impair visibility that further affects traffic safety and human activities while Tsai et al. (2003) reported PM_{10} is the major contributor to visibility deterioration.
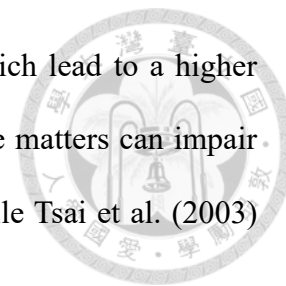
1.1.2 Importance of Secondary Organic Aerosol

The aerosol composition has regional variation and may have distinct effects on the atmosphere. With the aerosol mass spectrometer (AMS) analysis of the regional aerosol composition, organic aerosol (OA) is comprised of half of the submicron aerosol over most of 37 field studies. Secondary organic aerosol (SOA) is a major component of OA based on the concentration of oxygenated OA and hydrocarbon-like OA (Zhang et al., 2007). Due to the significant portion and complex physical properties of organic species, SOA might have a different effect compared with the current understanding of the aerosol effect. Though SOA is recently considered in the global model studies, the detailed chemical and physical properties of SOA remain uncertain. With the uncertainty of biogenic VOCs (BVOC) oxidation (halved and doubled yield), the annual global mean direct and first indirect radiative effects of SOA are estimated to be from -0.08 to -0.33 (W m^{-2}) and from -0.04 to -0.07 (W m^{-2}), respectively (Scott et al., 2014). In the future projection, Zhu et al. (2017) reported that global SOA would increase by 6.8% in mass under the RCP8.5 scenario and would still have its impact on the environment.

SOA is composed of low volatility organic species, generated from chemical reactions of volatile organic compounds (VOCs) after emitted from lands, via condensing on pre-existing particles or nucleating to generate new particles (i.e., new particle formation). In contrast, primary organic aerosol (POA) forms by directly emitted particles from ground activities such as fossil fuel combustion and forest fire. Recently, SOA is

widely concerned due to its potential effects on weather, climate, air quality, and human health as well as the uncertainty of its influences (Hallquist et al., 2009).
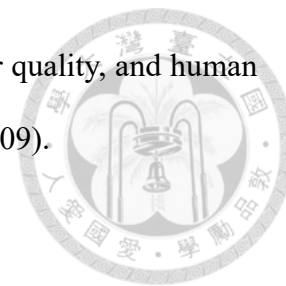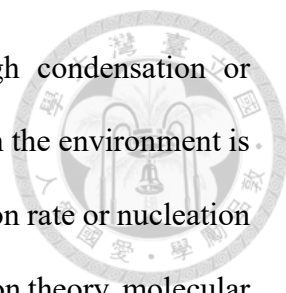
1.1.3 Oxidation of VOCs

The VOC oxidation is the essential step of SOA formation as there are many oxidants in the atmosphere, such as ozone (O_3), NO_3 radicals, and OH radicals (Chapleski et al., 2016). Ozone reacting with unsaturated hydrocarbon (i.e., olefin, a kind of VOCs) is the so-called ozonolysis reaction. According to Criegee (1975), the ozonolysis has multistep pathways to generate chemical species with carbonyl groups such as ketones, aldehydes, and acids which have lower volatility than that of reactants (Kroll & Seinfeld, 2008). The low volatile products can condense on pre-existing particles or nucleate to form SOA. During the ozonolysis, the so-called Criegee intermediates (CI), produced from the decomposition of 5-membered-ring primary ozonide, can undergo various reaction channels to form the distinct products. Furthermore, recent studies (Mauldin et al., 2012; Newland et al., 2015) reported that the stabilized CI (sCI) can produce H_2SO_4 by oxidizing SO_2 directly or indirectly with OH radicals formed from the unimolecular reaction of sCI. As a consequence, the ozonolysis of VOCs plays an important role in various chemical processes in the troposphere.

1.1.4 Atmospheric Nucleation

Atmospheric nucleation, a phase transition from the gas phase to the condensed phase (i.e. particle phase), produces new particles after the emitted precursor gases transform to the species with lower volatility through chemical reactions such as VOCs ozonolysis. Nevertheless, this process is energetically unfavorable and thus it requires sufficient supersaturation to overcome the energy barrier of forming the critical embryo
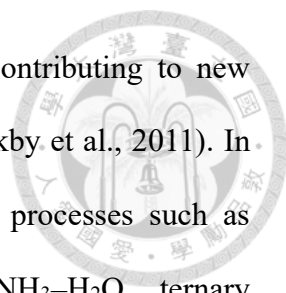
(cluster). The more stable clusters can continue to grow through condensation or coagulation processes if the saturation ratio of condensable species in the environment is higher than that on the surface of the clusters. A new particle formation rate or nucleation rate can be estimated from many methods such as dynamical nucleation theory, molecular dynamics, and classical nucleation theory (CNT) (Zhang et al., 2012). The dynamic nucleation theory evaluates the evaporation and condensation rate of the nucleation process using variational transition theory which is based on the molecular electronic structure. For molecular dynamics, the sampling of several molecular movements under periodic boundary conditions is conducted with Newtonian mechanics. Since this energy of sampling follows the Boltzmann distribution, the simulation might be computationally expensive to receive a nucleation event due to the high energy barrier of clustering. The classical nucleation theory estimates the homogeneous nucleation rate by evaluating the Gibbs free energy change of cluster formation as well as the collision rate between critical embryo and monomer with gas kinetics. The equation for calculating the CNT nucleation rate (Seinfeld & Pandis, 2016) is shown as Eq. 1:

$$J = \left(\frac{2\sigma}{\pi m_1}\right)^{\frac{1}{2}} \frac{v_1 N_1^2}{S} exp\left[-\frac{16\pi v_1^2 \sigma^3}{3(k_B T)^3 (\ln S)^2}\right] \tag{1}$$

where J (# cm^{-1} s^{-1}) is the nucleation rate; m_1 (g molecule^{-1}) is the molecular weight; v_1 (cm^3 molecule^{-1}) is the molecular volume; N_1 (molecule cm^{-3}) is the ambient number concentration of monomer; σ (dyne cm^{-1}) is the bulk surface tension; S is the saturation ratio; k_B is Boltzmann constant, and T (K) is temperature. The variables with subscript 1 indicate the monomer properties of nucleating species. With this CNT equation, one can easily estimate the nucleation rate from the bulk properties of nucleating species. However, it could lead to a large error due to a lack of detailed molecular interactions.

1.1.5 New Particle Formation

4
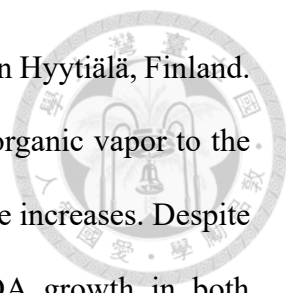
Sulfuric acid has long been considered as a major species contributing to new particle formation (NPF) in the troposphere (Sipilä et al., 2010; Kirkby et al., 2011). In most of the atmospheric models, sulfuric acid related nucleation processes such as H_2SO_4–H_2O binary homogeneous nucleation and H_2SO_4–NH_3–H_2O ternary homogeneous nucleation are parametrized and widely applied. Most of these nucleation models are CNT-based; nevertheless, they severely overpredict or underpredict the nucleation rate under some conditions and have unrealistic temperature sensitivity (Semeniuk & Dastoor, 2018).

Besides, organic compounds are recently considered to play an important role in atmospheric nucleation (Zhang et al., 2004; Riccobono et al., 2014). In laboratory studies, oxidation of specific VOCs can cause the new SOA formation; for instance, oxidizing the monoterpenes (a kind of VOCs which is a common emission from vegetation) such as α-pinene, β-pinene, and limonene by both OH radicals and ozone (Zhao et al., 2015). In field studies, a nocturnal NPF over the Landes forest was observed in the summer of 2015 according to Kammer et al. (2020). In this case, monoterpenes were strongly emitted by forest under the condition of hydric or thermic stress and then underwent ozonolysis to produce lower-volatility organic compounds relating to this NPF event. Therefore, NPF involving VOCs oxidation undoubtedly has a contribution to the global aerosol sources. However, these NPF resulting from pure organic nucleation are neglected in most of air quality model due to poor-understanding of its mechanism.

1.1.6 Particle Growth of SOA

Particles can grow up via coagulation or condensation processes and further become cloud condensation nuclei which modulate the cloud formation. According to the observation with an aerosol mass spectrometer (Riipinen et al., 2012), the uptake of low

5
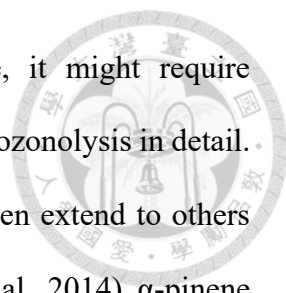
volatility organic vapor dominated the particle growth after the NPF in Hyytiälä, Finland. Ehn et al. (2014) also emphasized the importance of low volatility organic vapor to the condensational growth while its contribution raises as the particle size increases. Despite increased understanding, improvements of models simulating SOA growth in both laboratory and field studies are still necessary (Hallquist et al., 2009).

The driving force of the condensation process is the concentration difference between ambient and particle surface saturated concentrations. The Kelvin curvature effect will increase the surface saturated concentration of nanoparticles as compared with the activity in the particle phase determined by Raoult's law. Moreover, the accommodation coefficient determines the proportion that particle uptakes the colliding vapor molecule with a range of 0.1 to 1.0 among several studies (Liu et al., 2019). Besides the gas-diffusion-related terms mentioned above, particle-phase diffusion can also modulate particle growth (Zaveri et al., 2018; Zaveri et al., 2020). For monoterpene-deriving SOA, Renbaum-Wolff et al. (2013) and Ullmann et al. (2019) reported a high viscosity as a semisolid or glass-like scenario. According to Stokes-Einstein relation, higher viscosity of particle leads to a lower bulk diffusivity, and that makes particle hard to reach an equilibrium in gas-particle partitioning unlike a fast equilibrium process in liquid-like aerosols (such as aqueous inorganic aerosols). Therefore, the current existing model for simulating common aqueous inorganic aerosols might not be directly adapted to illustrate the particle growth of SOA.

1.2 Motivation and Goal

The NPF of monoterpenes ozonolysis was observed in both field and laboratory studies, but most atmospheric models do not take into account this NPF due to limited information. The pure-organic-nucleating SOA might be a source of new particles,

especially in forests (Semeniuk & Dastoor, 2018). Furthermore, it might require significant computing resources to describe the whole monoterpenes ozonolysis in detail. Model development should start from the significant species and then extend to others step by step. According to the BVOC emission model (Sindelarova et al., 2014), α-pinene is the dominant emitted compound (34%) among the monoterpenes for 1980 – 2010 with a global mean emission of 32 ± 1 Tg yr^{-1}. Also, Taiwan, a subtropical island with forest occupying 58% of the total area, had monoterpene emission estimated at 0.065 Tg yr^{-1} in 1999 (Chang et al., 2005). The topography and the α-pinene emission factor of Taiwan are shown in Fig. 1. One can perceive that significant emission factor of α-pinene over the higher altitude area, which is dominated by forest. Based on these statements, α-pinene ozonolysis involving NPF might be a potential source of nanoparticles globally. Hence, the quantification of organic NPF processes should be developed to further evaluate its impacts on the environment through model studies.

In this study, NPF from α-pinene ozonolysis in two distinct experimental setups (α-pinene-limiting environmental chamber study and ozone-limiting flow tube reactor study) was studied in the laboratory and simulated with the model solving the dynamic partitioning of gases to size-distributed aerosol. The nucleation rate applied to the Model for Simulating Aerosol Interactions and Chemistry (MOSAIC) (Zaveri et al., 2008; Zaveri et al., 2014) was derived from the classical nucleation theory (CNT) with adjusted parameters. With the processes of chemical reactions, nucleation, condensation, and coagulation, the simulated aerosol size distribution was compared with the experimental results to retrieve the optimal parameters and properties of products for further application to the atmospheric chemistry related models.

7

Chapter 2   Methodology

2.1 Harvard Environmental Chamber Experiment

The α-pinene ozonolysis at various relative humidities was investigated using a continuously mixed flow reactor, Harvard Environmental Chamber (HEC), which consists of 4.7 m^3 Teflon bag (Shilling et al., 2008). The schematic diagram for the setup is shown in Fig. 2. The inlets of gaseous flow rate are regulated with mass flow controllers while there was a constant removal flow with a residence time of ~4.5 hours. For α-pinene, a liquid sample was injected by a syringe pump and fully evaporated in a zero-air flow. Ozone was produced from zero air passing through an ultraviolet lamp. The humidified flow was generated by passing through an ultrapure water bubbler. The different relative humidity can be prepared by adjusting the flow rate of this humidifier flow. The ozone concentration, relative humidity, and temperature in the chamber were monitored during the experiments while α-pinene was only measured before the addition of ozone using a proton-transfer-reaction time-of-flight mass spectrometer with a concentration of 20.0 ppbv. The ozone was monitored by a UV absorption analyzer and reported at ~ 350.0 ppbv (during the experiment). The temperature was held around 22.0 ºC (295.15 K), and relative humidity increased stepwise ranging from < 1% to 75%.

New particle formation can be observed in this experiment without seeding. For particulate matter, the size distribution is measured every 5 minutes with a scanning mobility particle sizer (SMPS) consisting of a differential mobility analyzer (DMA) and condensation particle counter (CPC). The principle of SMPS is explained in detail in section 2.2.3. A high-resolution time-of-flight aerosol mass spectrometer was used to monitor the chemical composition of SOA. The HEC experiments were performed by S.T.

8

Martin group at Harvard University.

2.2 Flow Tube Reactor Experiment

The setup of the flow tube reactor (FTR) experiment for α-pinene ozonolysis is similar to that of Peng (2017). The whole system is housed the lab where the temperature was controlled at 298 ± 2 K. Experiments were performed at various ozone concentrations (limiting reagent) at relative humidity < 1%.

2.2.1 Experimental Setup

The setup of the FTR experiment is shown in Fig. 3. The air flow was supplied by an air compressor passing through the FT-IR purge gas generator (Model 75-62, Parker) where humidity, aerosol, and carbon dioxide were filtered out. The flow was controlled by digital mass flow controllers and entered into the pipeline where was constructed with Teflon tubes and a quartz FTR. The reaction was considered to be terminated after passing through a diffusion dryer with ozone scrubber and silica gel acting as ozone and water scavenger. Particulate matter was monitored by an SMPS system for number size distribution.

2.2.2 Gaseous Preparation and Reaction

The total mixed flow rate was regulated to 1.6 Lpm, with only 0.3 Lpm air flow entering quartz FTR and the excess flow was exhausted. For reactant preparation, 0.08 Lpm of air flow passed through a 185 nm pen-ray UV lamp to generate ozone, and the initial concentration was probed with a UV-Vis spectrometer (UV-1700, Shimadzu) at the wavelength of 254 nm. Initial ozone concentration was estimated by applying Beer's law with the absorbance measured from the UV-Vis spectrometer. The α-pinene vapor was

9

introduced to the system by passing 0.02 Lpm of air flow through the headspace of a glass bottle partially filled with liquid α-pinene (Sigma-Aldrich, 98 %) in an ice-water bath. The different air flow streams with reactants were mixed with 1.5 Lpm of dry air as a buffer flow. The initial concentration of α-pinene was estimated to be as 19.3 ppmv, while ozone was controlled at 46.01, 48.79, 67.74, and 87.90 ppbv for different experiments. The reaction time in FTR was estimated at 60 s, and the transport time from the diffusion dryer to SMPS is 12 s.

2.2.3 Aerosol Measurement

The size distribution of particulate matter produced from the reaction in the FTR experiment was probed with an SMPS (TSI Incorporated, Minnesota) including an Electrostatic Classifier (EC, Model 3080) with a nano DMA (Model 3085) and an Ultra-fine Condensation Particle Counter (UCPC, Model 3776). Particles first enter EC and carry some charges following a bipolar charge distribution by colliding with bipolar ions in an aerosol neutralizer (TSI 3077 with [85]Kr). Particles with the different charge-to-mass ratios are classified by an electric field of nano DMA with multi-charge correction in instrument manager software. Also, by applying 3.0 Lpm sheath flow and 0.3 Lpm sample flow, particles with size ranging from 4.0 nm to 156.0 nm can be analyzed. In UCPC, monodisperse particles pass through a capillary and mixed with clean sheath air flow carrying the n-butanol vapor which is vaporized in a heated saturator at 310 K and then diffuses out from there. The mixture of particle sample and n-butanol vapor are introduced into a cooled condenser where n-butanol vapor reaches a supersaturation and condenses on the particles. Eventually, the growth of the particle sample makes particles large enough to be probed and counted by an optical detector.

2.3 Model Description

In this study, MOSAIC was applied to simulate NPF for the given experiments. An earlier version of MOSAIC is one of the aerosol schemes in the Weather Research Forecasting model coupled with Chemistry (WRF-Chem). MOSAIC uses rigorous solvers to integrate the stiff ordinary differential equations (ODEs) such as gas-phase reactions and gas-aerosol phase partitioning. For instance, double-precision Livermore solver for the ordinary differential equations is used for the former, and the adaptive step time-split Euler method for the latter. In the following simulation, this study aimed to obtain an optimal nucleation rate and other parameters such as accommodation coefficients and bulk diffusivity mainly for HEC experiments. Also, the FTR experiments were taken into account in the comparison of simulation and experimental results to see the validity in a different system.

2.3.1 Conditions and Parameters Setup

Conditions of MOSAIC in this study were set based on the experimental setup without the addition of particles, as summarized in Table 1. New particles were generated from the function described in section 2.3.3. However, the range of particle size in the model was broader than that in experiments due to the addition of nucleation mode particles and the accumulation of the last bin under the mass conservation routine. Therefore, the simulation setup of HEC had particles ranged from 4.0 nm to 4000.0 nm with 175 bins, while the experimental results of HEC ranged from 10.6 nm to 495.8 nm with 108 bins. The simulations were performed for 9 days with a timestep of 6 s. For the FTR experiment, the conditions and parameters of the model were set to as close as possible to that of FTR experiments. The particle size in simulation ranged from 4.3 nm to 776.8 nm with 145 bins, while the experimental results of FTR ranged from 4.0 nm to

11

156.0 nm with 101 bins. The simulations were performed for 60 s with a timestep of 6 ms.

2.3.2 Chemical Reactions

According to Zhang et al. (2015), products of the α-pinene (formula: $C_{10}H_{16}$) ozonolysis probed by mass spectrometry are very diverse. Therefore, the products are classified as extremely low-volatile, low-volatile, semi-volatile, and volatile organic compounds (ELVOCs, LVOCs, SVOCs, and VOCs) in order of increasing volatility. The overall reactions of α-pinene ozonolysis are briefly demonstrated in Fig. 4. However, it is computationally expensive and complicated to simulate all chemical reactions with detailed chemical species. For simplicity, the two-products reaction (LVOC and SVOC) was applied in MOSAIC as Eq. 2:

$$C_{10}H_{16} + O_3 \rightarrow 0.14 \text{ LVOC} + 0.37 \text{ SVOC} \tag{2}$$
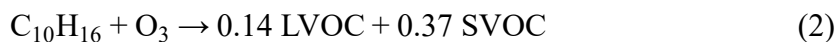
where 0.14 and 0.37 are the yields for LVOC and SVOC respectively. The reaction rate constant is expressed as the Arrhenius equation in Eq. 3:

$$k = (1.01 \times 10^{-15}) \times e^{-732.0/T} \tag{3}$$

where rate constant k equals 8.46×10^{-17} (cm^3 molecule^{-1} s^{-1}) at 295.15 K which is the average temperature in HEC. The applied physical parameters of LVOC and SVOC are summarized in Table 2. To simulate the reactants were nearly at steady-state in HEC, both concentrations of α-pinene and ozone remain constant, and that of other species (e.g. LVOC and SVOC) can be varied with reaction, nucleation, condensation and so on. However, the concentration of α-pinene in the model was set at 1.5 ppbv as a steady-state approximation with the presence of ozone. Furthermore, the influence of possible reactant heterogeneity inside the chamber on the particle size distribution concentration was

12

investigated. In this test, α-pinene concentration is modified as a time-dependent sinusoidal wave with a fixed ozone concentration.

2.3.3 Nucleation Process

In MOSAIC, there are only two homogenous nucleation processes as $H_2SO_4 – H_2O$ binary nucleation and $H_2SO_4 – H_2O – NH_3$ ternary nucleation. These nucleation rates are obtained from the previous study and parameterized. However, the model lacks the organic nucleation process; thus, it cannot illustrate well the new particle formation from α-pinene ozonolysis. Therefore, the nucleation process of organics is certainly needed to be constructed in MOSAIC. In this two-products system, LVOC is assumed to dominate the whole nucleation process owing to its low volatility. For simplicity, the nucleation rate of LVOC was illustrated using the CNT equation described in Eq.1. In modified MOSAIC, the nucleation rate is the function of monomer concentration (i.e. gaseous LVOC in this study). Most constants in Eq.1 can be obtained or derived from parameters in MOSAIC except the surface tension. The nucleation rate as a function of nucleating species concentration for different surface tensions of a critical embryo is shown in Fig. 5. At a given monomer concentration, the nucleation rate increases as the surface tension decreases.

The surface tension of pure α-pinene was reported as 25.7 dyne cm^{-1} at room temperature (Hritz et al., 2016; Wagner et al., 2019); however, that of LVOC in this system is unknown. Though Hritz et al. (2016) measured the surface tension of particles from α-pinene ozonolysis using atomic force microscopy and reported as 27.5 dyne cm^{-1} at RH < 10% under the experimental condition different from that of HEC. Nevertheless, the surface tension of LVOC should be similar to these values. To obtained an optimal surface tension of LVOC in HEC experiments, sensitivity tests of various surface tension

13

were performed. In the model simulation, the number density of new particles and the composition of new particles should be determined to illustrate the nucleation process. Besides, the diameter of the new particle was assumed to be around 4 nm as the first bin. The nucleation process was solved with the forward Euler algorithm. The number density of the new particles is calculated with Eq. 1 and then added to the first bin in every step. The consumption of gaseous LVOC during the nucleation process was considered to ensure the mass conservation of the system.

2.3.4 Condensation Process

The condensation process is a mass transfer from the gas phase to the particle phase and thus makes particles grow. An ordinary equation describing the rate of single-particle mass change owing to condensation can be written as Eq. 4 (Seinfeld & Pandis, 2016):

$$\frac{dm}{dt} = \frac{4\pi R_p D_{g,i} M_i}{RT}\left(P_i - P_{eq,i}\right)f(Kn_i, \alpha_i) \tag{4}$$

where m is the mass of a particle; R_p is the particle radius; $D_{g,i}$ is the gas-phase diffusivity of condensing species i; M_i is the molar weight; $P_i - P_{eq,i}$ is the difference between ambient vapor pressure and saturated pressure at particle surface; $f(Kn_i, \alpha_i)$ is the transition regime correction factor proposed by Fuchs and Sutugin (1971) as described in Eq.5.

$$f(Kn_i, \alpha_i) = \frac{0.75\alpha_i(1+Kn_i)}{Kn_i(1+Kn_i)+0.283\alpha_i Kn_i+0.75\alpha_i} \tag{5}$$

In the Eq. 5, Kn_i is the Knudsen number equal to $Kn_i = \lambda_i / R_p$ where λ_i is the mean free path, and α_i is the accommodation coefficient which means the proportion ($0 \leq \alpha_i \leq 1$) of incoming gaseous molecules attaching to the particle surface. The transition regime correction factor as a function of particle diameter for different accommodation

14

coefficients α is shown in Fig. 6. With the Eq. 4, one can explain that the vapor molecules condense on a particle by gaseous diffusion during this process. Note that there is no chemical reaction in particle phase, so only the evaporation process (i.e., $P_{eq,i} > P_i$) cause mass loss of particles.

To generalize to a polydisperse aerosol system with m size bins and number density N_m of each bin, rate of concentration $A_{i,m}$ (mole cm^{-3}) change of species i in a single particle needs to be calculated by rearranging and dividing Eq. 5 by the volume of a spherical particle with a radius equal to $R_{p,m}$:

$$\frac{dA_{i,m}}{dt} = \frac{D_{g,i}}{3R_{p,m}^2}\left(C_{g,i} - C_{g,i}^s\right)f(Kn_i, \alpha_i) \tag{6}$$

where $C_{g,i}$ is the ambient gaseous concentration and that with superscript s is the effective vapor concentration of particle surface calculated with Raoult's law and Kelvin equation describing the curvature effect. By multiplying the total volume density (cm^3 cm^{-3}) of the same radius, we can obtain the rate of concentration $C_{a,i,m}$ (mole cm^{-3}) change of particles in the air:

$$\frac{dC_{a,i,m}}{dt} = 4\pi R_{p,m}N_m D_{g,i}\left(C_{g,i} - C_{g,i}^s\right)f(Kn_i, \alpha_i) \tag{7}$$

Eq.7 is similar to that of Zaveri et al. (2014) while the particle-phase chemical reaction is neglected and diffusivity term around the interface between gas and particle-phase needs to be modified. In Zaveri et al. (2014), bulk diffusivity of particles is considered in MOSAIC which is reported that it might be an important factor modulating the particle growth (Zaveri et al., 2018; Zaveri et al., 2020). By applying two-film theory which describes the diffusive mass transfer with gas-side and particle-side films at the interface, Eq.7 can be written as follows:

$$\frac{dC_{a,i,m}}{dt} = 4\pi R_{p,m}^2 N_m K_{g,i}\left(C_{g,i} - C_{g,i}^s\right) \tag{8}$$

where $K_{g,i}$ is the overall gas-side mass transfer coefficient (cm s^{-1}) as shown in Eq.9.

$$K_{g,i} = \frac{k_{p,i}k_{g,i}}{k_{p,i}+k_{g,i}\left(\frac{C_{g,i}^*}{\Sigma_j A_j}\right)} \tag{9}$$

where, $C_{g,i}^*$ is the standard saturated vapor concentration of species i; $\Sigma_j A_j$ is the total concentration of all species in particle. The definition of gas-side and particle-side mass transfer coefficient ($k_{g,i}$ and $k_{p,i}$ respectively) is as follows:

$$k_{g,i} = \frac{D_{g,i}f(Kn_i,\alpha_i)}{R_{p,m}} \tag{10}$$

$$k_{p,i} = \frac{5D_{b,i}}{R_{p,m}} \tag{11}$$

In brief, the partitioning from the gas phase to particle phase in MOSAIC is propagated with Eq. 8 by using the adaptive step time-split Euler method.

In this study, both LVOC and SVOC gases can condense on particles except the precursors. In terms of the aerosol phase, products can only evaporate from particle surface or diffuse in the particle without any particle-phase reaction. The gaseous diffusivity of both species is assumed to be 0.05 cm^2 s^{-1}, and bulk diffusivity of particles ranged from $10^{-6} - 10^{-17}$ cm^2 s^{-1} for sensitivity tests. Also, the accommodation coefficients of the ozonolysis products were tuned to mainly fit the mode size of particle size distribution observed in HEC experiments. However, the Kelvin effect which can lower the condensation process especially on small particles was currently turned off by default. Simulation with the Kelvin-effect-related module turned on forcibly has been performed but there was a fatal problem about water activity. The water activity equaled ambient relative humidity immediately with low hygroscopicity which is not physically

reasonable. Therefore, the growth rate for small particles might be overestimated during the simulation.

2.3.5 Coagulation Process

The coagulation process in MOSAIC is propagated with the algorithm proposed by Jacobson (2002) and Jacobson et al. (1994). In this algorithm, two particles collide with each other by Brownian motion without a concentration gradient (Jacobson, 2005). The Brownian collision kernel ($K^B_{i,j}$) for i-size particle and j-size particle in the transition regime is shown as Eq. 12:

$$K^B_{i,j} = 4\pi(R_{p,i} + R_{p,j})(D_{a,i} + D_{a,j})/F \qquad (12)$$

where R_p, $D_{a,i}$, and F are the particle radius, particle diffusivity in the air, and the correction term, respectively. If F = 1, $K^B_{i,j}$ is the Brownian collision kernel for particles in the continuum regime; however, in this case, F can be written as:

$$F = \frac{R_{p,i} + R_{p,j}}{R_{p,i} + R_{p,j} + \sqrt{\delta_i^2 + \delta_j^2}} + \frac{4(D_{a,i} + D_{a,j})}{(R_{p,i} + R_{p,j})\sqrt{\bar{v}_i^2 + \bar{v}_j^2}} \qquad (13)$$

where δ_i is the distance describing two spherical particles approaching toward each other considering mean free path. Particle diffusivity in air $D_{a,i}$ is shown below:

$$D_{a,i} = \frac{k_B T}{6\pi R_{p,i} \eta_{air}} G_i \qquad (14)$$

where η_{air} is the air viscosity; G_i is the Cunningham slip-flow correction factor as shown in Eq. 15.

$$G_i = 1 + Kn_{a,i}\left[1.249 + 0.42exp\left(-0.87/Kn_{a,i}\right)\right] \qquad (15)$$

With the coagulation process, small particles are consumed and adhered to larger particles.

17

The overall effect of coagulation reduces the total number density without changing the total volume of the particle (i.e., mass conservation). It is worthwhile to mention that the efficiency of coagulation could be less than one owing to the van de Waal force or other interactions between two particles in some researches (Hou et al., 2020).
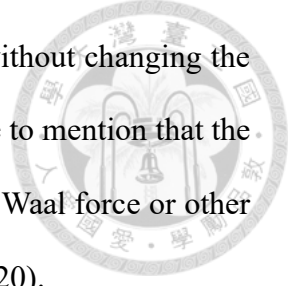
2.3.6 Removal Process

Considering the continuous removal flow in HEC, the function that the number concentration of both gas and particle except reactants (i.e. α-pinene and ozone) changes with time was treated as a first-order exponential decay with 4.5 hours lifetime. Besides, particle, especially ultrafine particle, can adhere to the wall of a chamber or tube which is so-called wall loss. The wall loss correction (WLC) is indispensable in this kind of NPF experiment because the SOA yield may be underestimated; however, WLC was temporarily neglected when simulating the HEC experiments due to the low surface-to-volume ratio of the chamber (Wang et al., 2018). However, WLC is necessary when simulating the FTR experiments due to the high surface-to-volume ratio of the reactor. The penetration P (Hinds, 1999) was calculated to estimate WLC in the model and shown below:

$$P = 1 - 5.5\mu^{2/3} + 3.77\mu, for\ \mu < 0.009 \tag{16}$$

$$P = 0.819\ e^{-11.5\mu} + 0.0975\ e^{-70.1\mu}, for\ \mu \geq 0.009 \tag{17}$$

$$\mu = D_a dt/\pi R_t^2 \tag{18}$$

where; D_a is the particle diffusivity in the air which is size-dependent; dt is the time-step used in the model; R_t is the radius of FTR. In every time-step, number concentrations of each bin were multiplied by P and that means particles can partially adhere everywhere when passing through the FTR.

Chapter 3　Results and Discussion
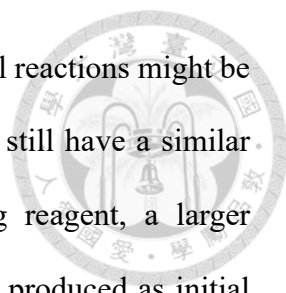
3.1　Experimental Results

3.1.1　HEC Experiments

The HEC experiment was performed from 2017/12/19 to 2018/01/14 with ascending relative humidity step, and the experimental data with relative humidity 15% is shown in Fig. 7. In general, an apparent steady-state was reached with the balance of continual NPF, condensation, and removal processes. The total number density roughly remained at 3.6 $\times 10^3$ (# cm^{-3}) with ~ 10% of fluctuation during the period. It is worthwhile to mention that there was an obviously strong NPF around 10 a.m. on 25th Dec immediately as there was a sudden drop in ozone concentration (likely caused by a temporal control failure issue), as shown in Fig. 8. A decrease of the reactant can lead to weaker NPF and weaker particle growth owing to slower product formation. As the ozone was back to a more stable condition, the NPF raised again with a larger magnitude due to less existing particles to lead the accumulation of low-volatile gas species. However, the next NPF was suppressed as there was a significant amount of particles to increasing the condensation, and the total number reached a similar dynamic steady-state as that before the concentration turbulence.

3.1.2　FTR Experiments

Fig. 9 shows the size distributions of the FTR experimental results for different initial ozone concentrations. The total number density and mode size for these experiments incorporated with previous work (Peng, 2017) is also shown in Fig. 10. The small differences between the two works might mainly result from the trace impurities of

the carrier air or the possible environmental fluctuation. The chemical reactions might be slightly altered during the experiments, but the results of this work still have a similar trend with the previous one. Because ozone acted as a limiting reagent, a larger concentration of condensable vapors (e.g., LVOC and SVOC) were produced as initial ozone concentration raised. The nucleation process can be therefore enhanced by a larger amount of nucleating species such as LVOC. Also, an increased concentration of SVOC can afford the overall particle growth despite the stronger nucleation process. Consequently, larger mode size and total number density at higher initial ozone concentration were observed in these experiments.

3.2 Results of the Control Simulation

The CNT surface tension, accommodation coefficient, and bulk diffusivity were focused in this study. The MOSAIC model lacked the definition of LVOC's surface tension (i.e. CNT surface tension), so the sensitivity test of that was performed to obtain the optimal one. Both the accommodation coefficient and bulk diffusivity widely discussed in recent studies modulate the particle growth. These two parameters were also adjusted to fit the HEC experimental result; therefore, sensitivity tests for that were conducted as well. With CNT surface tension of 23.0 dyne cm^{-1}, bulk diffusivity of 10^{-12} $cm^2\,s^{-1}$, and accommodation coefficients of 0.1 and 0.3 for LVOC and SVOC respectively, the simulation as the control run of this study gave the most optimal result for simulating HEC experiments. The size distribution evolution of the control run incorporated with that observed in HEC experiments is shown in Fig. 11. At the beginning of the simulation, extremely strong nucleation occurred owing to the weak condensation of low particle surface area (Fig. 12). With constant reactant concentrations, both particle size distribution and product concentration were able to reach a steady-state gradually. When

20

simulation time larger than ~72 hrs, the fluctuation of gaseous product concentrations reduced to 0.1%. To ensure simulations reach a steady-state, the last frame of that at 216 hrs was chosen to do further analysis, discussion, and comparison with experimental results.
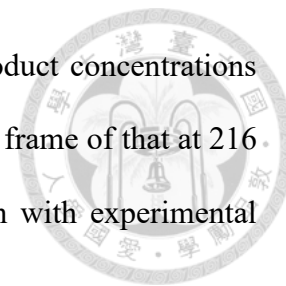
3.3 Sensitivity Tests

3.3.1 Surface Tension of CNT Nucleation Rate

In these tests, surface tensions of the CNT nucleation rate range from 22.0 to 24.0 dyne cm^{-1}. The size distributions of simulation with different CNT surface tensions are shown in Fig. 13. At the same LVOC concentration, lower surface tension results in a higher nucleation rate, and thus the total number density is larger for sure. However, it can, therefore, restrain the condensation process and result in a smaller mode size for the particle size distribution. Besides, similar simulation results with various accommodation coefficient of SVOC are shown in Fig. 13 – 17.

As compared with the experimental results, nucleation rates with CNT surface tension ranging from 22.5 to 23.5 dyne cm^{-1} seem to be optimal for the size distribution simulation. However, larger surface tensions for α-pinene and particles from α-pinene ozonolysis (25.7 and 27.5 dyne cm^{-1}, respectively) were reported by Hritz et al. (2016). The discrepancy between these surface tensions can be explained by the following possible reasons: (1) different experimental setups might lead to the various chemical composition of particles; (2) lower surface tension of nanoparticle can be illustrated by Tolman surface tension correction. The surface tension of particles in the vapor-liquid heterogeneous system is subject to the curvature of particles with the following Tolman (Eq. 19) and Gibbs (Eq. 20) corrections (Tolman, 1949; Xue et al., 2011):

$$\frac{\sigma}{\sigma_\infty} = \frac{1}{1+2\delta_\infty/R_s} \tag{19}$$

$$\frac{\sigma}{\sigma_\infty} = e^{-2\delta_\infty/R_s} \tag{20}$$

where σ is the surface tension of particles and that with subscript ∞ is the surface tension of planar surface; δ_∞ is the Tolman length; R_s is the effective radius of surface tension which is slightly smaller than the radius of the droplet R_p by the distance of molecular monolayer. By assuming the planar surface tension σ_∞ of 27.5 dyne cm^{-1}, the surface tension is reduced to around 25 dyne cm^{-1} on the particles with diameter of a 4.0 nm, the assumed embryo size (Fig. 18). Therefore, the optimal CNT surface tensions are reasonable as compared to other bulk studies with Tolman surface tension correction.

3.3.2 Accommodation Coefficient

The condensation process can be enhanced by increasing the accommodation coefficients (α). The simulation results with different coefficient sets are shown in Fig. 19. For a given α_{LVOC}, a higher α_{SVOC} will lead to a larger mode size owing to the stronger condensation. However, the titration of LVOC caused by increased uptake of SVOC can further enhance the LVOC partitioning process. The increased partition of LVOC vapor to the particle-phase can, therefore, suppress the nucleation process. In contrast, a higher α_{LVOC} can significantly reduce the gas-phase LVOC concentration and weaken the nucleation process. The total number density was dramatically decreased as shown in Fig. 19. Besides, the mode size increases more significantly than the simulation with a higher α_{SVOC} because condensing vapor can only partition into fewer particles. Based on these tests, α_{LVOC} was fixed at 0.1 for the following studies to approach a similar mode size as the observation.
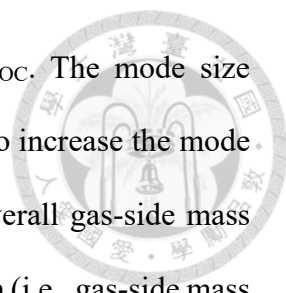
Fig. 20 shows the particle size distribution for different α_{SVOC}. The mode size increases as the coefficient increases; however, there is a limitation to increase the mode size by tuning α_{SVOC} which can be explained using Eq. 9 of the overall gas-side mass transfer coefficient. While the accommodation coefficient related term (i.e., gas-side mass transfer coefficient) is large enough, the overall mass transfer coefficient, which is proportional to the mass transfer rate remains nearly the same. Therefore, it is not necessary to lavishly raise the accommodation coefficients of SVOC to enhance the growth rate. In recent studies, some accommodation coefficients of the organic molecules were obtained from both simulation and laboratory observation. Julin et al. (2014) estimated the accommodation coefficients for simple organic molecules such as adipic acid ($HCOO(CH_2)_4COOH$) and n-nonane ($CH_3(CH_2)_7CH_3$) as 1.0 with MD simulation. In a laboratory study of Liu et al. (2019), the accommodation coefficient of organic nitrate (also a kind of LVOC or SVOC) partitioning into pre-existing particles such as ammonium sulfate or α-pinene/O_3 SOA were estimated and mostly in the range of 0.5 to 1.0. Though the accommodation coefficients used in this study are lower than those reported in the researches mentioned above, its effect on the size distribution of simulation is small within this order. Consequently, this factor is the fine-tuning term and should be in the range between 0.1 to 1.0 for further simulation.

3.3.3 Bulk Diffusivity

Molecules with low bulk diffusivity (or diffuse in high viscosity particle) would have significantly reduced condensation on particles when the surface of the particle is occupied with the same chemical species. The condensation becomes thermodynamically unfavorable to slow down particle growth. In recent studies, SOA was reported to be in a glass-like or semi-solid scenario with extremely low intraparticle diffusivity (Renbaum-

23

Wolff et al., 2013; Zaveri et al., 2018). The reported diffusivity from different studies ranged widely from 10^{-14} to 10^{-17} cm^2 s^{-1}. Without considering the concentration gradient, the timescale τ for a molecule diffusing from surface to center of a particle with a coefficient D_b can be written as:

$$\tau = \frac{R_p^2}{\pi^2 D_b} \tag{21}$$

Therefore, compared with the growth of small particles, that of large particles can be suppressed by diffusive limitation which means large particles spend more time to reach particle-phase equilibrium.

To investigate the effect of bulk diffusivity (D_b) on NPF, sensitivity tests with different bulk diffusivity were performed and the size distribution of that is shown in Fig. 21 with detailed information summarized in Table 4. For D_b ranging from 10^{-6} to 10^{-14} cm^2 s^{-1}, size distribution slightly shifted toward large particles with similar total number density as D_b decreased. For $D_b < 10^{-14}$ cm^2 s^{-1}, the size distribution has a different trend and more sensitive to D_b. This phenomenon can be explained by the definition of the overall gas-side mass transfer coefficient with D_b ranging from 10^{-6} to 10^{-14} cm^2 s^{-1}. The increased mode size as D_b decreased might be due to the partitioning process controlled through kinetics or thermodynamics. For the gas species partitioning into a single particle, as shown in Fig. 22, plenty of SVOC condenses fast on new particles with high bulk diffusivity, indicating the "kinetic partitioning process". In contrast, LVOC can condense more with sufficient time owing to slow particle growth, and that indicated the "thermodynamic partitioning process". Furthermore, considering the polydisperse particles, the thermodynamic partitioning process leads to weaker nucleation but stronger condensation.

24

Nevertheless, nonlinear changes of size distribution were obtained with bulk diffusivity < 10^{-14} cm^2 s^{-1} and seem counterintuitive based on the discussion above. When particle growth was restricted by the extremely low bulk diffusivity, both LVOC and SVOC were accumulated in the gas phase. Therefore, high gaseous LVOC resulted in that the strength of NPF rebounded at bulk diffusivity of 10^{-15} cm^2 s^{-1}. To sum up, bulk diffusivity of the particles can indirectly modulate the NPF by either positive or negative feedback for the HEC experiments.

3.3.4 The Fluctuation of Reactant Concentration

Considering the possible inhomogeneity in the HEC experiment, the simulations of fluctuating reactant concentrations were performed in this study. Because α-pinene in the HEC experiment is the limiting reagent and more likely subject to this inhomogeneous issue, multi-sinusoidal waves as a function of time were applied to modify the ODE of α-pinene concentration with two cases as Eq. 22 and 23 in Fig. 23:

$$C1(t) = 1.5 + 0.0046 \sin\left(\frac{\pi}{1} \times t\right) \ (ppbv) \tag{22}$$

$$C2(t) = 1.5 + 0.014 \sin\left(\frac{\pi}{6} \times t\right) + 0.0023 \sin\left(\frac{\pi}{1} \times t\right) \ (ppbv) \tag{23}$$

Both modifications contain "small fluctuation" with a period of 2 hours while only $C2$ contains "big fluctuation" with a period of 12 hours; the α-pinene concentration with these modifications will merely fluctuate within 1.3% during the simulation. The size distribution evolution of simulations and HEC experiment are shown in Fig. 24. The discrete NPF can be achieved with both simulations though there are still significant discrepancies between the experiment and simulations. Therefore, one may infer that the inhomogeneity of the reactant concentrations in the HEC can cause the fluctuation of

25

particle size distribution. This result also indicates that nucleation in this system is sensitive to the precursor concentration. The spatial inhomogeneity of gas and aerosol concentration should be both taken into account; one can also obtain an accurate frequency of fluctuation by analyzing the number density of specific bin or ozone concentration with Fourier transform.

3.3.5 Comparison with HEC Experimental Results

To evaluate the goodness-of-fit to HEC experimental results, root-mean-square error (RMSE) and mean relative error (MRE) of size were introduced applied for the evaluation:

$$SSE = \sum_{i=1}^{Total\ bin} \left\{ \left[\frac{dN(i)}{dlogDp} \right]_{HEC} - \left[\frac{dN(i)}{dlogDp} \right]_{SIM} \right\}^2 \tag{24}$$

$$RMSE = \sqrt{\frac{SSE}{Total\ bin}} \tag{25}$$

$$MRE = \frac{1}{Total\ bin} \sum_{i=1}^{Total\ bin} \frac{\left| \left[\frac{dN(i)}{dlogDp} \right]_{HEC} - \left[\frac{dN(i)}{dlogDp} \right]_{SIM} \right|}{\left[\frac{dN(i)}{dlogDp} \right]_{HEC}} \tag{26}$$

The RMSE and MRE analysis results are summarized in Table 5 and Table 6, respectively. The simulation gives the lowest error in RMSE analysis with CNT surface tension of 23.0 dyne cm^{-1}, and the lowest MRE with CNT surface tension of 23.5 dyne cm^{-1}. Therefore, five size distributions of the simulations with the lower error in MRE analysis are compared with each other and shown in Fig. 26. As mentioned in section 3.3.2, results with the same CNT surface tension (23.0 dyne cm^{-1}) but different accommodation coefficients (0.3, 0.4, and 0.5) have similar size distribution with that of observed in HEC experiments. Whereas, results with CNT surface tension of 23.5 dyne cm^{-1} both have a huge gap in number density around 200 nm particle diameter. The reason is that MRE

estimates the error with the percentage of number density instead of exact value so it could underestimate the exact error of the bins with large number density while RMSE analysis is more reliable.
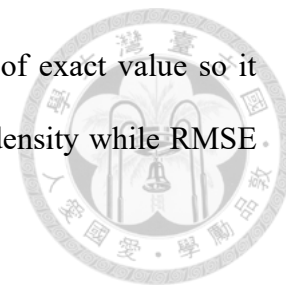
Consequently, simulation with CNT surface tension of 23.0 dyne cm^{-1} and accommodation coefficients of LVOC and SVOC equal to 0.1 and 0.3, respectively is the most optimal condition to illustrate the HEC experiment. The nucleation rate at a steady state is estimated as 0.305 # cm^{-3} s^{-1} with the parameters stated above. Nevertheless, it still underestimates the number density of particle size around mode size and overestimates the other bins. That indicates small particles should grow faster while large particles should have a slower growth rate. A recent study (Zaveri et al., 2018) with a lower bulk diffusivity for the accumulation mode particles (diameter with hundreds of nanometer) than that for the Aitken mode (diameter of tens of nanometer) showed a good agreement with the experimental results. For further adjustment of this model, a similar procedure can be applied tentatively; otherwise, the model cannot longer give better results with the current tuned parameters in this study. Moreover, particle-phase reaction or yield of products can be taken into consideration in the future.

3.4 Simulating the FTR Experiments

In the following discussion, the simulation results of the last frame at 60 s were compared to the experimental results. Unlike α-pinene-limiting ozonolysis in HEC experiments, ozone is the limiting reagent in FTR experiments. To test the validity for the reaction with different limiting reagent, the same nucleation curve obtained above was applied to simulate the FTR experiments. Besides, a steady-state assumption for reactants does not apply to the FTR simulations because the reactant concentration continued reducing through the flow tube. The simulation results with different initial ozone

concentrations are shown in Fig. 27. The simulation shows a similar mode size but one order of magnitude higher in number concentration than the results from the FTR experiment, even with the possible WLC taken into account (Fig. 29). Besides, simulations with 4% of initial α-pinene concentration (772 ppbv) were performed (Fig. 28) considering the uncertainty that α-pinene vapor in the bottle might not reach to the saturation concentration. Also, despite similar total number density of model with reduced initial α-pinene concentration to the experimental results, the mode size failed to match up with that observed in FTR experiments.

To explain this discrepancy, one can start from the yields of both LVOC and SVOC according to the mechanism of ozonolysis. According to the reaction model proposed by Kamens et al. (1999), OH radicals can oxidize the ozonolysis products and might further reduce their volatility. α-pinene, as an excess reagent in the FTR experiment, can also react with OH radical (Henry et al., 2012) and then compete with the ozonolysis products. As a result, there is a hypothesis that some SVOCs produced during ozonolysis evolving into LVOCs through OH oxidation channel might be inhibited by an abundance of α-pinene. The yield of LVOC might be therefore smaller than that in the HEC experiment. On the contrary, the yield of SVOC might be larger than that in the HEC experiment because more SVOC can be produced from the OH oxidation channel. Hence, the overall LVOC to SVOC yield ratio could be smaller compared to the current one used in this study. If decreasing the LVOC/SVOC ratio in the two-products model, simulation with weaker nucleation and stronger condensation will make mode size shift toward larger diameter. Though there were some uncertainties for yield issue, one thing that can be confirmed is this two-products model coupled with the CNT nucleation rate is not suitable for FTR experiments.
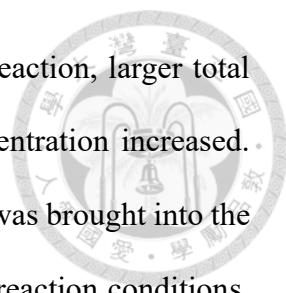
3.5 Uncertainties of the Model

As an atmospheric chemistry model, the performance of simulating a large time scale and steady-state system such as the environmental chamber is comparable in particle number density. However, there were some uncertainties in this model. For instance, this model neglected the Kelvin effect of SOA, which can suppress particle growth, especially for liquid-like nanoparticles. Under the Kelvin effect, the smaller particles tend to evaporate instead of growing up due to higher saturated concentration on the surface. Consequently, underestimating the number density of the particle diameter around mode size in HEC experiments might be even worse considering this effect. On the other hand, if the SOA is solid-like in reality, this effect can be excluded in the model. Besides, the dimerization of products in the particle phase can raise the particle growth on the contrary. However, the module of dimerization is currently turned off to avoid the model being too complicated in the early stage of adopting the organic nucleation curve. Otherwise, this particle-phase reaction is a common phenomenon reported in recent researches (Zaveri et al., 2018) and is necessary to apply to this model. Furthermore, the effect of humidity is lacked in this organic NPF model while it could alter the gas-phase reactions and particle growth. An increase of RH might reduce the oxidation efficiency of ozonolysis (Peng, 2017) and enlarge the bulk diffusivity (Renbaum-Wolff et al., 2013). Though the humidity effect might be weak due to low RH of the cases investigated in this study, NPF with larger RH should be taken into consideration for the real atmosphere.

Chapter 4 Conclusion

In this study, the nucleation rates for α-pinene ozonolysis products were derived from CNT to illustrate the NPF observed in both HEC and FTR experiments. Besides, the sensitivity tests were performed to investigate the effect of different parameters, such as CNT surface tension, accommodation coefficients, and bulk diffusivity. With this work, the model for the NPF from α-pinene ozonolysis might be able to apply to the current atmospheric chemistry model to illustrate this NPF in reality. The overall results of this study can be concluded as the following points:

1.   According to simulation results, not only increasing the CNT nucleation rate can enhance the NPF but also adjusting the factor of the condensation process can indirectly modulate the strength of nucleation. Mode size of size distribution can increase with less total number density change by increasing the accommodation coefficient of SVOC. However, as the bulk diffusivity further reduced to 10^{-15} cm^2 s^{-1}, the nucleation process was enhanced instead of being suppressed.

2.   For simulating NPF in HEC experiments, the nucleation curve with CNT surface tension of 23.0 dyne cm^{-1} seems the most optimal with bulk diffusivity of 10^{-12} cm^2 s^{-1} and accommodation coefficients of 0.1 and 0.3 for LVOC and SVOC respectively with a steady-state of the nucleation rate at 0.305 # cm^{-3} s^{-1}. However, this simulation underestimated the number density of particles with a diameter around mode size while overestimating that of others. By applying fluctuational waves into α-pinene concentration in the simulation, continual and discrete NPF observed in HEC experiments can be simulated. This phenomenon is likely due to the spatial inhomogeneity in the chamber, which might result from an instrumental glitch.

30

3.   In FTR experiments, derived from ozone-limiting ozonolysis reaction, larger total number density and mode size was observed as initial ozone concentration increased. Also, the same nucleation curve in simulating the HEC experiments was brought into the simulation of FTR experiments to examine the validity in different reaction conditions. Despite considering some uncertainties, this model seems not suitable for the ozone-limiting ozonolysis derived NPF compared to that with α-pinene-limiting in HEC experiments. The possible reason is that different reaction conditions (i.e. ozone-limiting vs. α-pinene-limiting) might alter the yield ratio of LVOC to SVOC which further influences the NPF. Therefore, the yield of both products needs modification to simulate FTR experiments more appropriately in the future.

4.   Although this model coupled with the organic nucleation curve had not a bad performance in simulating the size distribution of HEC experiments, there were still some uncertainties in the simulations. The neglect of the Kelvin effects for organics in this study might overestimate the particle growth of small particles. Therefore, the performance of simulating the HEC experiment could be worse if this effect was taken into account. Besides, the model in this study lacks other effects such as dimerization and humidity for organic NPF. Further investigation for these effects should be conducted to reduce the uncertainties.
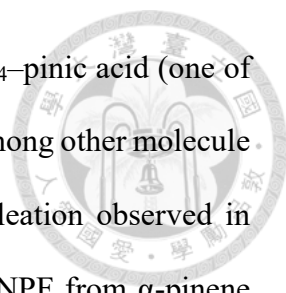
Chapter 5　Future Work
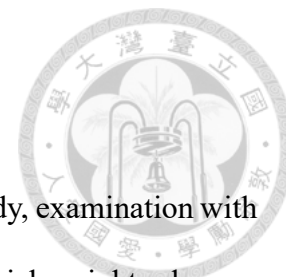
Besides further fine-tuning of parameters investigated in this study, examination with other modules in MOSAIC such as particle-phase reactions which might play an important role in particle growth might help improve the performance of simulation experiments. For instance, dimerization in particle-phase might slow down the evaporation of products in SOA (Zaveri et al., 2018). Furthermore, high molecular weight dimer ester in such α-pinene/O_3 SOA was observed in both field and laboratory studies, and its formation mechanism was also proposed recently (Kristensen et al., 2014; Zhang et al., 2015; Kristensen et al., 2016).

As mentioned in section 3.5, the effect of humidity was not considered in this study; however, it can somehow influence both particle growth and NPF. According to Renbaum-Wolff et al. (2013), the viscosity of SOA reduced as relative humidity increased while the particle surface tension raised owing to the water uptake of particles (Hritz et al., 2016). As the results of the previous FTR experimental study (Peng, 2017), NPF became weaker in the presence of water vapor which likely reacted with HO_2 radicals to form complex and further modulated the efficiency of oxidation. Therefore, the adjustments of moisture effect to this NPF model are indeed necessary to apply to regional or global models in the future.

As mentioned in section 1.1.5, H_2SO_4 derived NPF is a significant source of new particles in the world. Besides, the H_2SO_4-organic nucleation might be another new particle source which has seasonal variation driven by photochemical and biological mechanism (Riccobono et al., 2014). The model considering H_2SO_4-organic nucleation gave more negative first aerosol indirect radiative forcing, which indicated a stronger cooling effect (Scott et al., 2014). Furthermore, the association energy estimated from the
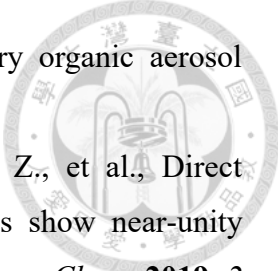
quantum chemistry calculation shown in Fig. 30 suggests that H_2SO_4–pinic acid (one of the major products in α-pinene ozonolysis) has stronger interaction among other molecule pairs. This calculation might be able to explain the enhanced nucleation observed in previous FTR experiments (Peng, 2017). Hence, a model study of NPF from α-pinene ozonolysis incorporating SO_2 (as a precursor of H_2SO_4) is important. However, the two-products model might not be suitable for this system owing to the omission of detailed reactions such as the production of OH radicals which can oxidize SO_2 to form H_2SO_4. Despite challenging work for the revising model, it is essential because of its potentially crucial contribution to revealing the mechanism of atmospheric nucleation in the presence of both anthropogenic and biogenic emission.
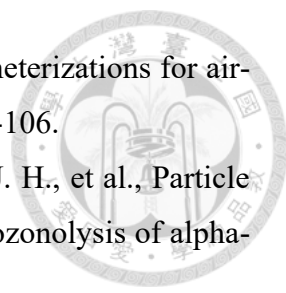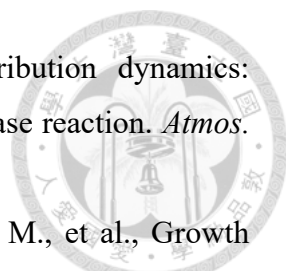
References

Albrecht, B. A., Aerosols, cloud microphysics, and fractional cloudiness. *Science* **1989,** *245* (4923), 1227-1230.

Becker, J.;   Sandwell, D.;   Smith, W.;   Braud, J.;   Binder, B., et al., Global bathymetry and elevation data at 30 arc seconds resolution: SRTM30_PLUS. *Mar. Geod.* **2009,** *32* (4), 355-371.

Bernstein, J. A.;   Alexis, N.;   Barnes, C.;   Bernstein, I. L.;   Nel, A., et al., Health effects of air pollution. *Journal of allergy and clinical immunology* **2004,** *114* (5), 1116-1123.

Chang, K.-H.;   Chen, T.-F.; Huang, H.-C., Estimation of biogenic volatile organic compounds emissions in subtropical island—Taiwan. *Sci. Total Environ.* **2005,** *346* (1-3), 184-199.

Chapleski, R. C.;   Zhang, Y.;   Troya, D.; Morris, J. R., Heterogeneous chemistry and reaction dynamics of the atmospheric oxidants, O 3, NO 3, and OH, on organic surfaces. *Chem. Soc. Rev.* **2016,** *45* (13), 3731-3746.

Criegee, R., Mechanism of ozonolysis. *Angew. Chem., Int. Ed. Engl.* **1975,** *14* (11), 745-752.

Ehn, M.;   Thornton, J. A.;   Kleist, E.;   Sipilä, M.;   Junninen, H., et al., A large source of low-volatility secondary organic aerosol. *Nature* **2014,** *506* (7489), 476-479.

Fuchs, N.; Sutugin, A., High-dispersed aerosols. In *Topics in current aerosol research*, Elsevier: 1971; p 1.

Hallquist, M.;   Wenger, J. C.;   Baltensperger, U.;   Rudich, Y.;   Simpson, D., et al., The formation, properties and impact of secondary organic aerosol: current and emerging issues. *Atmos. Chem. Phys.* **2009,** *9* (14), 5155-5236.

Henry, K. M.;   Lohaus, T.; Donahue, N. M., Organic aerosol yields from α-pinene oxidation: bridging the gap between first-generation yields and aging chemistry. *Environ. Sci. Technol.* **2012,** *46* (22), 12347-12354.

Hinds, W. C., *Aerosol technology: properties, behavior, and measurement of airborne particles*. John Wiley & Sons: 1999.

Hou, D.;   Zong, D.;   Lindberg, C. S.;   Kraft, M.; You, X., On the coagulation efficiency of carbonaceous nanoparticles. *J. Aerosol Sci.* **2020,** *140*, 105478.

Hritz, A. D.;   Raymond, T. M.; Dutcher, D. D., A method for the direct measurement of surface tension of collected atmospherically relevant aerosol particles using

atomic force microscopy. *Atmos. Chem. Phys.* **2016,** *16* (15), 9761-9769.

Jacobson, M. Z., Analysis of aerosol interactions with numerical techniques for solving coagulation, nucleation, condensation, dissolution, and reversible chemistry among multiple size distributions. *J. Geophys. Res.* **2002,** *107* (D19).

Jacobson, M. Z., *Fundamentals of atmospheric modeling*. Cambridge university press: 2005.

Jacobson, M. Z.;　Turco, R. P.;　Jensen, E. J.; Toon, O. B., Modeling coagulation among particles of different composition and size. *Atmos. Environ.* **1994,** *28* (7), 1327-1338.

Julin, J.;　Winkler, P. M.;　Donahue, N. M.;　Wagner, P. E.; Riipinen, I., Near-unity mass accommodation coefficient of organic molecules of varying structure. *Environ. Sci. Technol.* **2014,** *48* (20), 12083-12089.

Kamens, R.;　Jang, M.;　Chien, C.-J.; Leach, K., Aerosol formation from the reaction of α-pinene and ozone using a gas-phase kinetics-aerosol partitioning model. *Environ. Sci. Technol.* **1999,** *33* (9), 1430-1438.

Kammer, J.;　Flaud, P. M.;　Chazeaubeny, A.;　Ciuraru, R.;　Le Menach, K., et al., Biogenic volatile organic compounds (BVOCs) reactivity related to new particle formation (NPF) over the Landes forest. *Atmos. Res.* **2020,** *237*.

Kirkby, J.;　Curtius, J.;　Almeida, J.;　Dunne, E.;　Duplissy, J., et al., Role of sulphuric acid, ammonia and galactic cosmic rays in atmospheric aerosol nucleation. *Nature* **2011,** *476* (7361), 429-33.

Kristensen, K.;　Cui, T.;　Zhang, H.;　Gold, A.;　Glasius, M., et al., Dimers in α-pinene secondary organic aerosol: effect of hydroxyl radical, ozone, relative humidity and aerosol acidity. *Atmos. Chem. Phys.* **2014,** *14* (8), 4201-4218.

Kristensen, K.;　Watne, Å. K.;　Hammes, J.;　Lutz, A.;　Petäjä, T., et al., High-molecular weight dimer esters are major products in aerosols from α-pinene ozonolysis and the boreal forest. *Environ. Sci. Technol. Lett.* **2016,** *3* (8), 280-285.

Kroll, J. H.; Seinfeld, J. H., Chemistry of secondary organic aerosol: Formation and evolution of low-volatility organics in the atmosphere. *Atmos. Environ.* **2008,** *42* (16), 3593-3624.

Li, X.;　Chee, S.;　Hao, J.;　Abbatt, J. P.;　Jiang, J., et al., Relative humidity effect on the formation of highly oxidized molecules and new particles during monoterpene oxidation. *Atmos. Chem. Phys.* **2019,** *19* (3).

Librando, V.; Tringali, G., Atmospheric fate of OH initiated oxidation of terpenes.

Reaction mechanism of α-pinene degradation and secondary organic aerosol formation. *J. Environ. Manage.* **2005,** *75* (3), 275-282.

Liu, X.; Day, D. A.; Krechmer, J. E.; Brown, W.; Peng, Z., et al., Direct measurements of semi-volatile organic compound dynamics show near-unity mass accommodation coefficients for diverse aerosols. *Commun. Chem.* **2019,** *2* (1), 1-9.

Mauldin, R. L., 3rd; Berndt, T.; Sipila, M.; Paasonen, P.; Petaja, T., et al., A new atmospherically relevant oxidant of sulphur dioxide. *Nature* **2012,** *488* (7410), 193-6.

Newland, M. J.; Rickard, A. R.; Vereecken, L.; Muñoz, A.; Ródenas, M., et al., Atmospheric isoprene ozonolysis: impacts of stabilised Criegee intermediate reactions with SO2, H2O and dimethyl sulfide. *Atmos. Chem. Phys.* **2015,** *15* (16), 9521-9536.

Pöschl, U., Atmospheric aerosols: composition, transformation, climate and health effects. *Angewandte Chemie International Edition* **2005,** *44* (46), 7520-7540.

Peng, H.-W. A Study of New Particle Formation from Ozonolysis of α-Pinene. National Taiwan University, 2017.

Pope III, C. A.; Dockery, D. W., Health effects of fine particulate air pollution: lines that connect. *Journal of the air & waste management association* **2006,** *56* (6), 709-742.

Renbaum-Wolff, L.; Grayson, J. W.; Bateman, A. P.; Kuwata, M.; Sellier, M., et al., Viscosity of α-pinene secondary organic material and implications for particle growth and reactivity. *Proc. Natl. Acad. Sci.* **2013,** *110* (20), 8014-8019.

Riccobono, F.; Schobesberger, S.; Scott, C. E.; Dommen, J.; Ortega, I. K., et al., Oxidation products of biogenic emissions contribute to nucleation of atmospheric particles. *Science* **2014,** *344* (6185), 717-721.

Riipinen, I.; Yli-Juuti, T.; Pierce, J. R.; Petäjä, T.; Worsnop, D. R., et al., The contribution of organics to atmospheric nanoparticle growth. *Nature Geoscience* **2012,** *5* (7), 453-458.

Scott, C. E.; Rap, A.; Spracklen, D. V.; Forster, P. M.; Carslaw, K. S., et al., The direct and indirect radiative effects of biogenic secondary organic aerosol. *Atmos. Chem. Phys.* **2014,** *14* (1), 447-470.

Seinfeld, J. H.; Pandis, S. N., *Atmospheric chemistry and physics: from air pollution to climate change*. John Wiley & Sons: 2016.

Semeniuk, K.; Dastoor, A., Current state of aerosol nucleation parameterizations for air-quality and climate modeling. *Atmos. Environ.* **2018,** *179*, 77-106.

Shilling, J. E.; Chen, Q.; King, S. M.; Rosenoern, T.; Kroll, J. H., et al., Particle mass yield in secondary organic aerosol formed by the dark ozonolysis of alpha-pinene. *Atmos. Chem. Phys.* **2008,** *8* (7), 2073-2088.

Sindelarova, K.; Granier, C.; Bouarar, I.; Guenther, A.; Tilmes, S., et al., Global data set of biogenic VOC emissions calculated by the MEGAN model over the last 30 years. *Atmos. Chem. Phys.* **2014,** *14* (17), 9317-9341.

Sipilä, M.; Berndt, T.; Petäjä, T.; Brus, D.; Vanhanen, J., et al., The role of sulfuric acid in atmospheric nucleation. *Science* **2010,** *327* (5970), 1243-1246.

Stocker, T. F.; Qin, D.; Plattner, G.-K.; Tignor, M.; Allen, S. K., et al., Climate change 2013: The physical science basis. *Contribution of working group I to the fifth assessment report of the intergovernmental panel on climate change* **2013,** *1535*.

Tolman, R. C., The superficial density of matter at a liquid-vapor boundary. *J. Chem. Phys.* **1949,** *17* (2), 118-127.

Tsai, Y. I.; Lin, Y. H.; Lee, S. Z., Visibility variation with air qualities in the metropolitan area in southern Taiwan. *Water, Air, and Soil Pollution* **2003,** *144* (1-4), 19-40.

Twomey, S., The influence of pollution on the shortwave albedo of clouds. *J. Atmos. Sci.* **1977,** *34* (7), 1149-1152.

Ullmann, D. A.; Hinks, M. L.; Maclean, A. M.; Butenhoff, C.; Grayson, J. W., et al., Viscosities, diffusion coefficients, and mixing times of intrinsic fluorescent organic molecules in brown limonene secondary organic aerosol and tests of the Stokes–Einstein equation. *Atmos. Chem. Phys.* **2019**.

Wagner, Z.; Bendová, M.; Rotrekl, J.; Orvalho, S., Densities, Vapor Pressures, and Surface Tensions of Selected Terpenes. *J. Solution Chem.* **2019,** *48* (7), 1147-1166.

Wang, N.; Jorga, S. D.; Pierce, J. R.; Donahue, N. M.; Pandis, S. N., Particle wall-loss correction methods in smog chamber experiments. *Atmos. Meas. Tech.* **2018,** *11* (12), 6577-6588.

Xue, Y.-Q.; Yang, X.-C.; Cui, Z.-X.; Lai, W.-P., The effect of microdroplet size on the surface tension and Tolman length. *J. Phys. Chem. B* **2011,** *115* (1), 109-112.

Zaveri, R. A.; Easter, R. C.; Fast, J. D.; Peters, L. K., Model for Simulating Aerosol Interactions and Chemistry (MOSAIC). *J. Geophys. Res.* **2008,** *113* (D13).

Zaveri, R. A.; Easter, R. C.; Shilling, J. E.; Seinfeld, J. H., Modeling kinetic

partitioning of secondary organic aerosol and size distribution dynamics: representing effects of volatility, phase state, and particle-phase reaction. *Atmos. Chem. Phys.* **2014,** *14* (10), 5153-5181.

Zaveri, R. A.; Shilling, J. E.; Zelenyuk, A.; Liu, J.; Bell, D. M., et al., Growth Kinetics and Size Distribution Dynamics of Viscous Secondary Organic Aerosol. *Environ. Sci. Technol.* **2018,** *52* (3), 1191-1199.

Zaveri, R. A.; Shilling, J. E.; Zelenyuk, A.; Zawadowicz, M. A.; Suski, K., et al., Particle-Phase Diffusion Modulates Partitioning of Semivolatile Organic Compounds to Aged Secondary Organic Aerosol. *Environ. Sci. Technol.* **2020,** *54* (5), 2595-2605.

Zhang, Q.; Jimenez, J. L.; Canagaratna, M. R.; Allan, J. D.; Coe, H., et al., Ubiquity and dominance of oxygenated species in organic aerosols in anthropogenically-influenced Northern Hemisphere midlatitudes. *Geophys. Res. Lett.* **2007,** *34* (13).

Zhang, R.; Khalizov, A.; Wang, L.; Hu, M.; Xu, W., Nucleation and growth of nanoparticles in the atmosphere. *Chemical reviews* **2012,** *112* (3), 1957-2011.

Zhang, R.; Suh, I.; Zhao, J.; Zhang, D.; Fortner, E. C., et al., Atmospheric new particle formation enhanced by organic acids. *Science* **2004,** *304* (5676), 1487-1490.

Zhang, X.; McVay, R. C.; Huang, D. D.; Dalleska, N. F.; Aumont, B., et al., Formation and evolution of molecular products in alpha-pinene secondary organic aerosol. *Proc. Natl. Acad. Sci. U. S. A.* **2015,** *112* (46), 14168-73.

Zhao, D. F.; Kaminski, M.; Schlag, P.; Fuchs, H.; Acir, I. H., et al., Secondary organic aerosol formation from hydroxyl radical oxidation and ozonolysis of monoterpenes. *Atmos. Chem. Phys.* **2015,** *15* (2), 991-1012.

Zhu, J.; Penner, J. E.; Lin, G.; Zhou, C.; Xu, L., et al., Mechanism of SOA formation determines magnitude of radiative effects. *Proc. Natl. Acad. Sci. U. S. A.* **2017,** *114* (48), 12685-12690.

Tables

Table. 1 Conditions setup for simulating HEC and FTR experiments.

Conditions	HEC experiments	FTR experiments
Duration	216 hrs	60 secs
Time step (sec)	6.0	0.006
Temperature (K)	295.15	298.15
RH (%)	15.0	1.0
O3 conc. (ppbv)	350.0	46.01 – 87.90
α-pinene conc. (ppbv)	1.5	19300
Total size bins	175	145
Min bin size (nm)	4	4.3
Max bin size (nm)	4000	776.8

Table. 2 Parameters setup for LVOC and SVOC in all of the simulations.

Parameters	LVOC	SVOC
Yield of ozonolysis	0.14	0.37
Molecular weight (g mole^{-1})	250	200
Volatility (μg m^{-3})	0.01	1
Particle phase density (g cm^{-3})	1.4	1.4
Hygroscopicity κ	0.1	0.1

Table. 3 Total number density, mode size, and nucleation rate at steady state of the simulation with different CNT surface tension and accommodation coefficient α of SVOC.

CNT S.T. (dyne cm^{-1})	α_{SVOC}	Total number density (# cm^{-3})	Mode size (nm)	S.S. nucleation rate (# cm^{-3} s^{-1})
22.0	0.1	6943.98	142.5	0.670
	0.2	6681.50	154.2	0.612
	0.3	6524.82	160.4	0.578
	0.4	6416.31	166.8	0.555
	0.5	6335.92	166.8	0.538
22.5	0.1	5493.20	160.4	0.481
	0.2	5265.37	166.8	0.441
	0.3	5128.66	173.5	0.417
	0.4	5033.51	180.5	0.401
	0.5	4962.56	187.8	0.388
23.0	0.1	4342.79	173.5	0.351
	0.2	4146.20	187.8	0.322
	0.3	4027.98	195.3	0.305
	0.4	3945.29	203.2	0.294
	0.5	3883.56	203.2	0.285
23.5	0.1	3431.05	187.8	0.260
	0.2	3262.63	203.2	0.239
	0.3	3161.14	211.4	0.227
	0.4	3090.17	219.9	0.218
	0.5	3036.90	228.8	0.211
24.0	0.1	2709.21	203.2	0.195
	0.2	2565.82	219.9	0.179
	0.3	2479.42	238.0	0.170
	0.4	2419.03	247.5	0.163
	0.5	2373.54	257.5	0.159

40

Table. 4 The total number density, mode size, aerosol mass fraction of SVOC, and nucleation rate at steady state of simulation with different bulk diffusivity.

Bulk diffusivity D_b (cm^2 s^{-1})	Total number density (# cm^{-3})	Mode size (nm)	Mass fraction of SVOC (aer) (%)	S.S. nucleation rate (# cm^{-3} s^{-1})
10^{-06}	4030.41	195.3	67.919	0.3057
10^{-08}	4030.41	195.3	67.919	0.3057
10^{-10}	4030.36	195.3	67.919	0.3057
10^{-12}	4027.98	195.3	67.918	0.3052
10^{-13}	4006.10	195.3	67.913	0.3027
10^{-14}	3835.41	211.4	67.866	0.2818
10^{-15}	3424.93	247.5	67.523	0.2248
10^{-16}	4247.31	203.2	65.884	0.2664
10^{-17}	11612.05	131.6	61.749	0.9937

Table. 5 Root-mean-square error analysis between the size distribution of simulation and HEC experimental results. And, the bulk diffusivity of each simulation was the same as 10^{-12} cm^2 s^{-1}.

RMSE (# cm^{-3})		Accommodation coefficient of SVOC				
		0.1	0.2	0.3	0.4	0.5
Surface tension of CNT	22.0	1.73×10^3	1.59×10^3	1.50×10^3	1.45×10^3	1.41×10^3
	22.5	9.02×10^2	7.66×10^2	6.87×10^2	6.35×10^2	6.00×10^2
	23.0	3.97×10^2	3.40×10^2	3.26×10^2	3.28×10^2	3.36×10^2
	23.5	5.88×10^2	6.53×10^2	6.98×10^2	7.31×10^2	7.56×10^2
	24.0	9.74×10^2	1.05×10^3	1.10×10^3	1.13×10^3	1.16×10^3

Table. 6 Mean relative error analysis between the size distribution of simulation and HEC experimental results. And, the bulk diffusivity of each simulation was the same as 10^{-12} cm^2 s^{-1}.
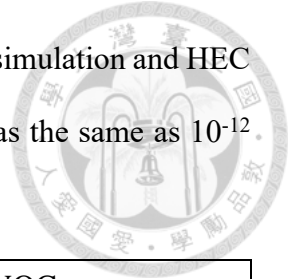
MRE (%)		Accommodation coefficient of SVOC				
		0.1	0.2	0.3	0.4	0.5
Surface tension of CNT	22.0	113.83	103.01	96.41	91.76	88.29
	22.5	63.59	54.43	48.85	44.90	41.95
	23.0	29.79	23.27	19.59	17.58	16.37
	23.5	18.59	18.65	20.16	22.44	24.79
	24.0	28.98	34.69	38.23	40.76	42.67

Table. 7 Total number density and mode size of FTR experiments and simulation results. For total number density of both simulations were corrected with 12 s WLC between diffusion dryer and SMPS.

Initial O3 conc. (ppbv)	FTR experiment		Simulation with α-pinene initial conc. = 19.3 ppmv		Simulation with α-pinene initial conc. = 772 ppbv	
	Total number density (# cm^{-3})	Mode size (nm)	Total number density (# cm^{-3})	Mode size (nm)	Total number density (# cm^{-3})	Mode size (nm)
46.01	9.76×10^3	21.7	3.82×10^6	36.4	4.35×10^4	4.6
48.79	3.27×10^4	26.9	3.85×10^6	36.4	5.35×10^4	4.6
67.74	1.88×10^5	37.2	4.08×10^6	39.1	1.64×10^5	4.6
87.90	3.78×10^5	42.9	4.23×10^6	42.0	3.81×10^5	4.6

Figures
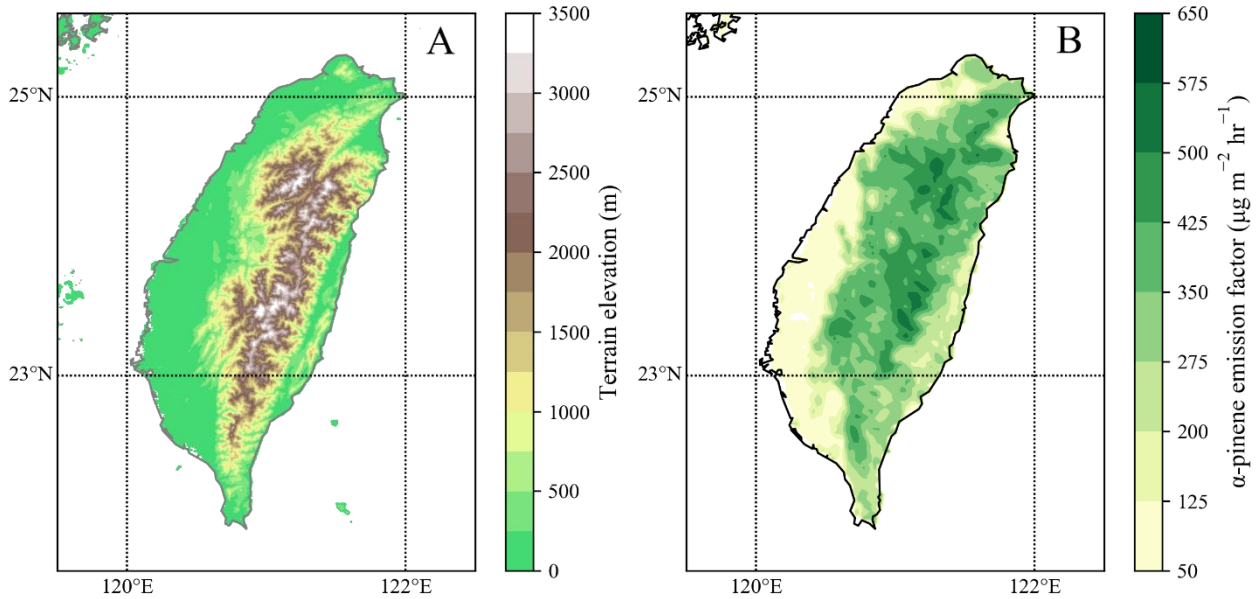
Fig. 1 (A) The terrain elevation of Taiwan plotted from the data of SRTM30 (Becker et al., 2009). (B) The spatial distribution of α-pinene emission factor of TEDS in Taiwan which is also the input data of MEGAN v2.04.
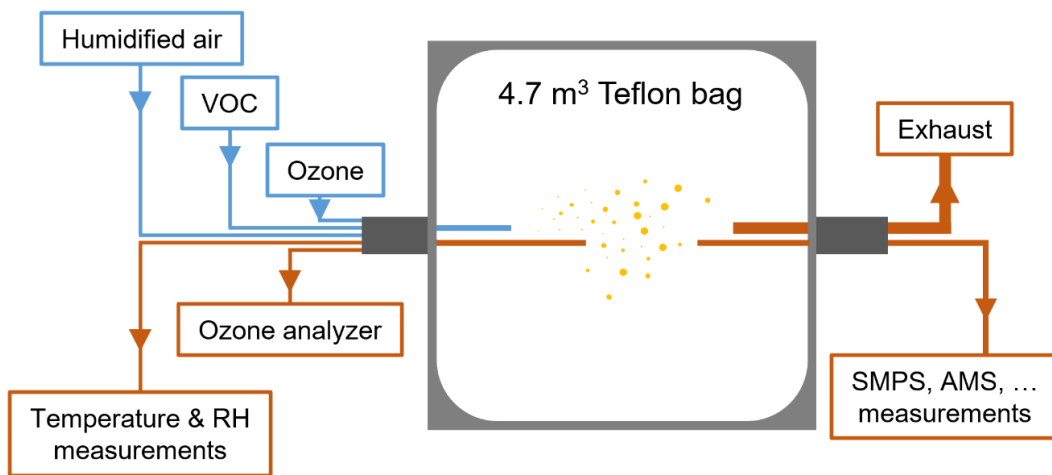
Fig. 2 The experimental setup of Harvard Environmental Chamber experiments.
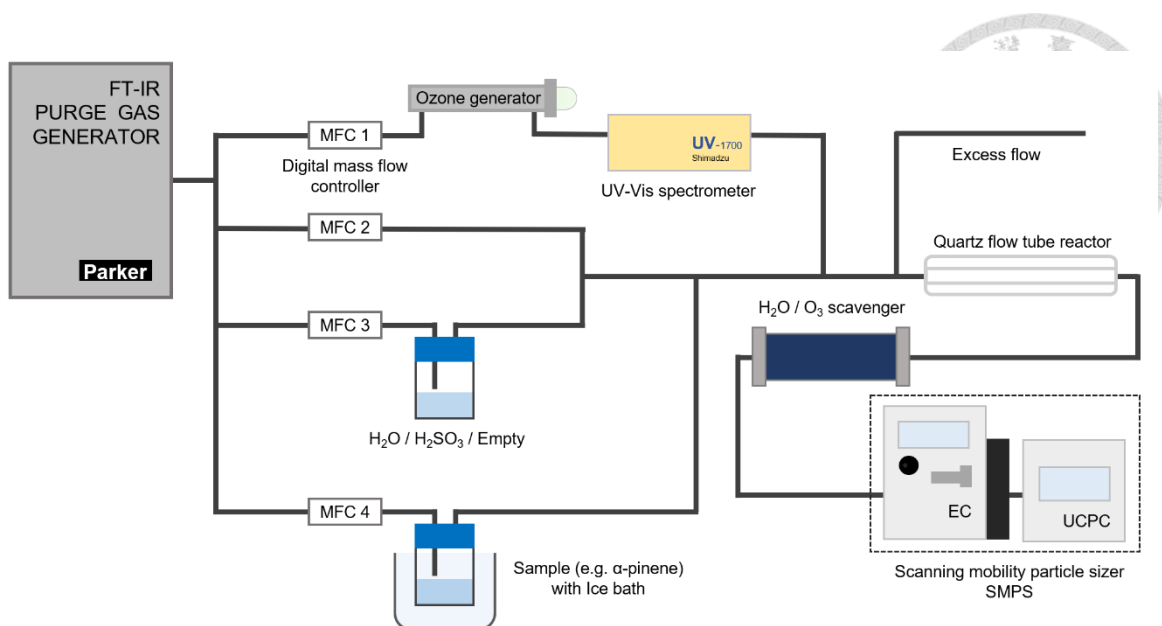
Fig. 3 The experimental setup of flow tube reactor experiments.
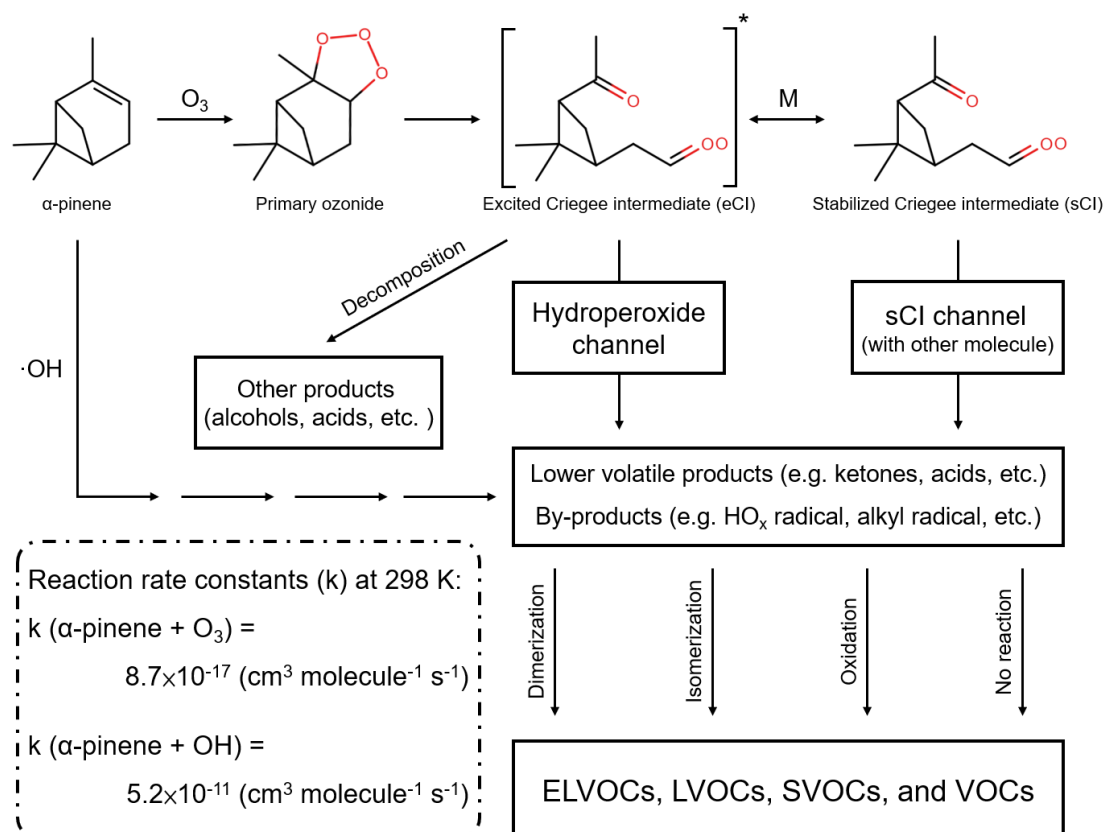
Fig. 4 Brief reaction pathways of α-pinene ozonolysis according to the previous studies (Librando & Tringali, 2005; Kristensen et al., 2014; Zhang et al., 2015; Li et al., 2019).
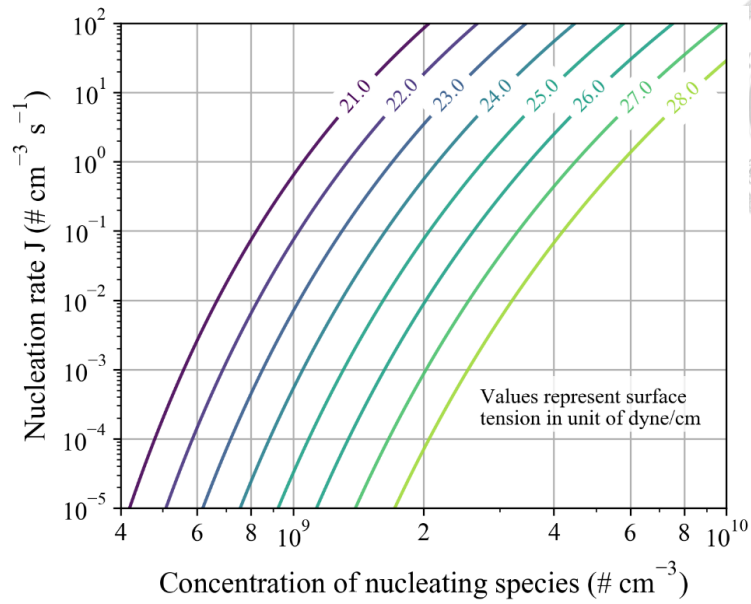
Fig. 5 Nucleation rate as a function of nucleating species concentration for different surface tensions derived from classical nucleation theory.
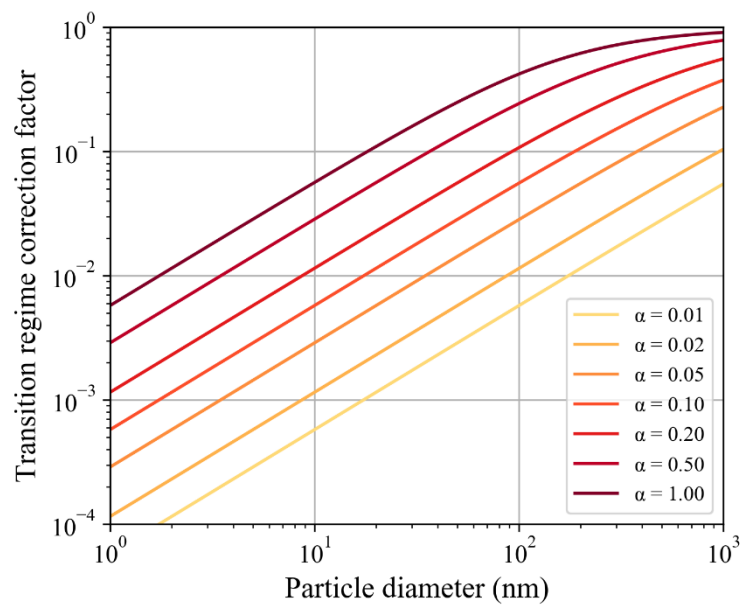
Fig. 6 The transition regime correction factor as a function of particle diameter for different accommodation coefficients α.

45
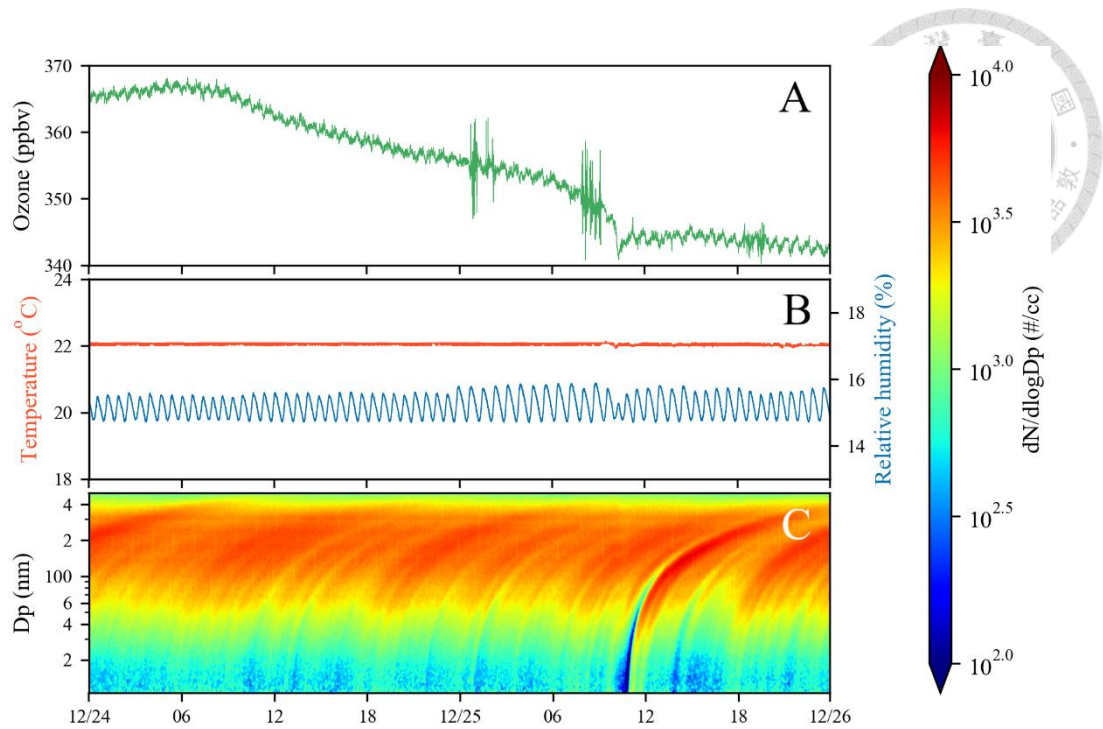
Fig. 7 The temporal profile of (A) ozone concentration, (B) temperature, relative humidity, and (C) particle size distribution monitored in HEC experiments.
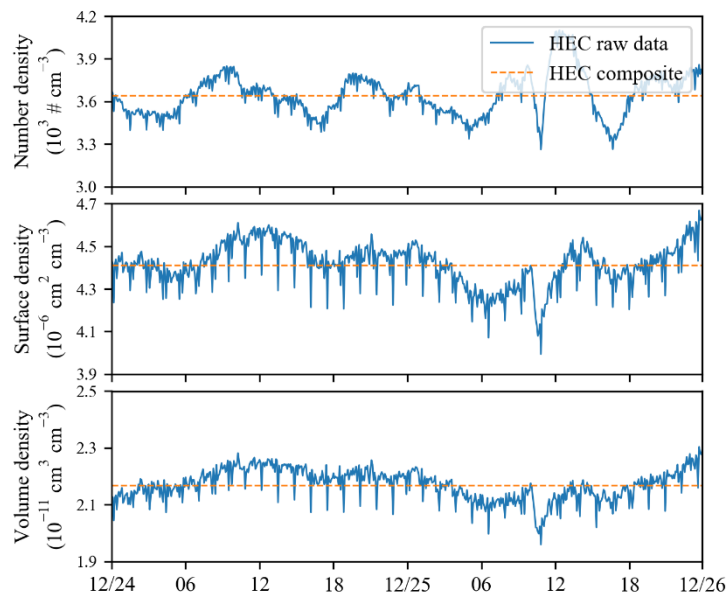
Fig. 8 Total number, surface area, and volume density of particle in HEC during the period with relative humidity of 15%. Each term with the label of HEC raw data is calculated from the size distribution given by SMPS measurement while that of HEC composite is the average size distribution during the period.

46
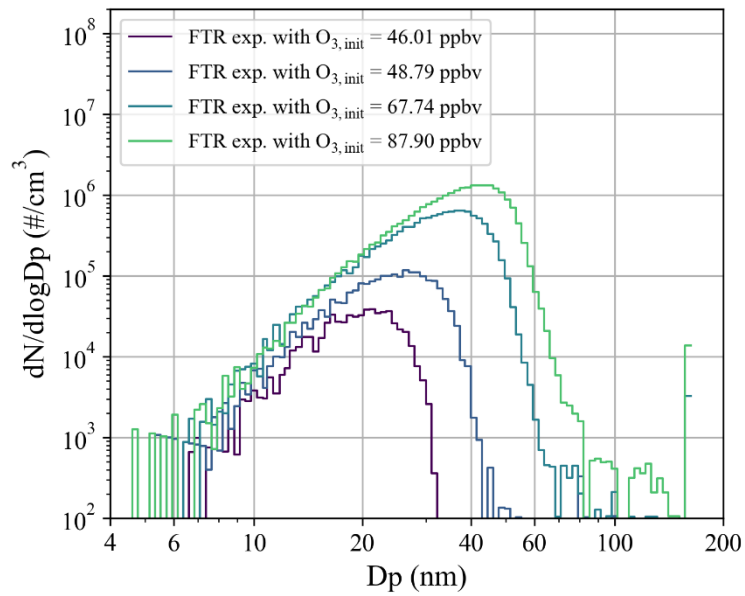
Fig. 9 The Size distribution of FTR experiments for different initial ozone concentrations. Condition: initial α-pinene concentration = 19.3 ppmv.
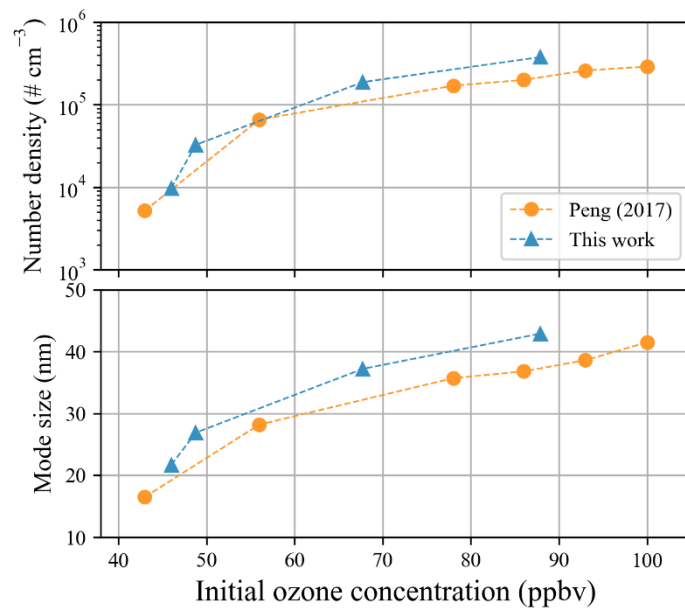
Fig. 10 The total number density and mode size of FTR experiments for different initial ozone concentrations incorporated with previous work (Peng, 2017). The preparation of α-pinene vapor in both works was the same and the initial concentration was estimated at 19.3 ppmv.
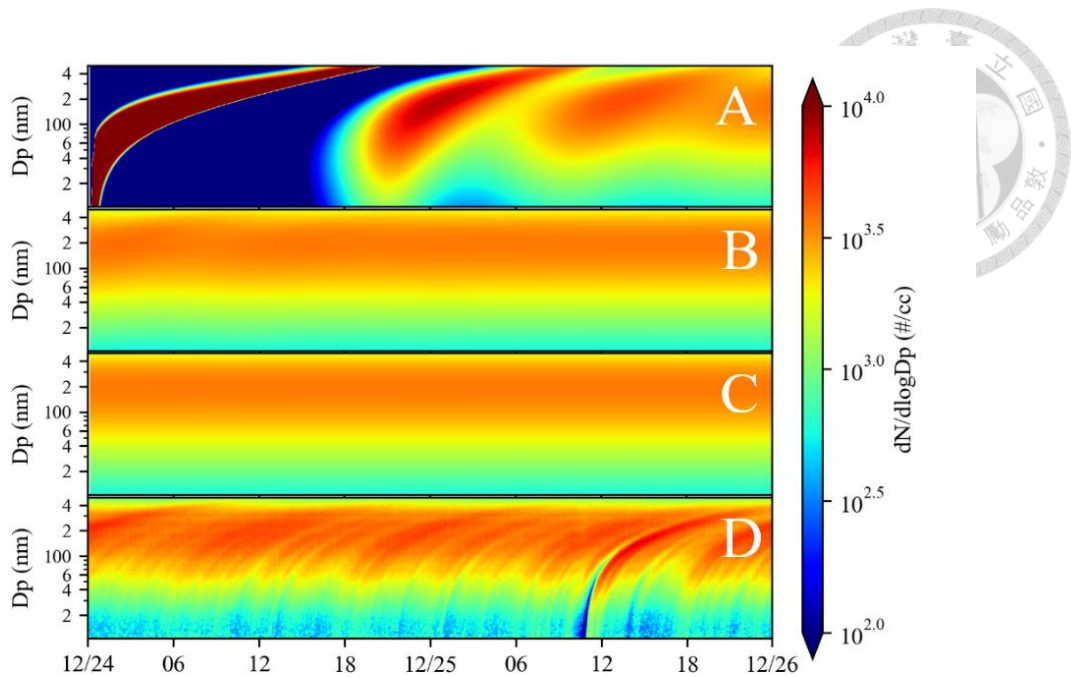
Fig. 11 The Size distribution evolutions of (A-C) control run of MOSAIC simulation and (D) HEC result observed from 2017/12/24 00:00 to 2017/12/26 00:00. The results of MOSAIC simulation represented in a time interval of (A) 0 – 48 hr, (B) 48 – 96 hr, and (C) 96 – 144 hr. Simulation parameters: surface tension of CNT nucleation = 23.0 dyne cm^{-1}, α_{LVOC} = 0.1, α_{SVOC} = 0.3, and bulk diffusivity = 10^{-12} cm^2 s^{-1}.
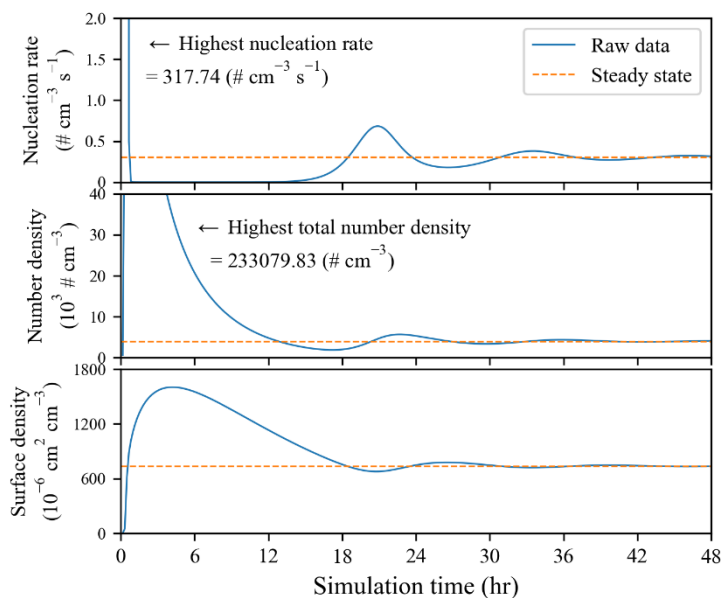
Fig. 12 Nucleation rate, total number density, and surface area density of particle in the first 48 hr simulation. The simulation result at 216 hr was assumed to be at steady state. Simulation parameters: surface tension of CNT nucleation = 23.0 dyne cm^{-1}, α_{LVOC} = 0.1, α_{SVOC} = 0.3, and bulk diffusivity = 10^{-12} cm^2 s^{-1}.
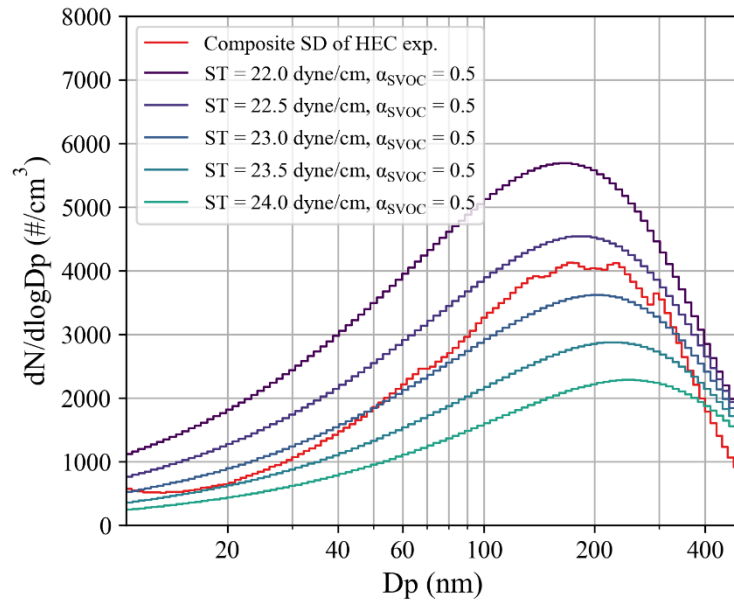
48
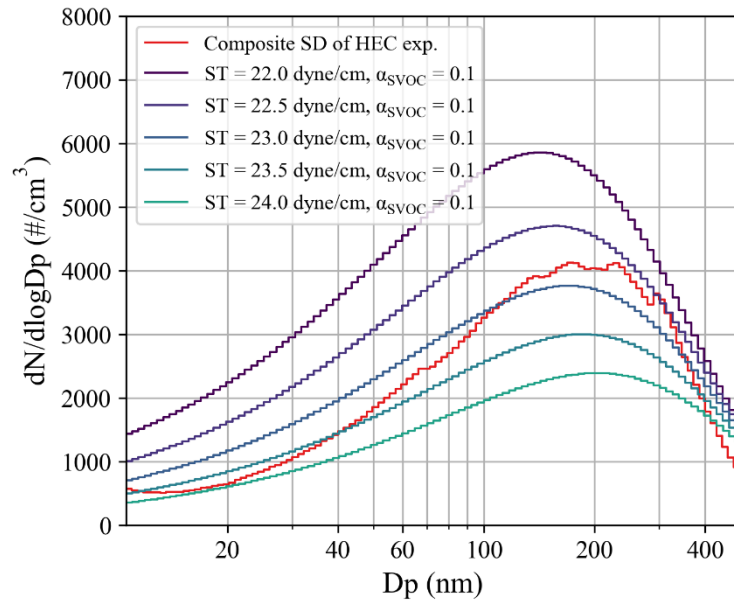
Fig. 13 The steady-state size distribution of simulation with different CNT surface tension incorporated with the composite size distribution of HEC experiments. Parameters: α_{SVOC} = 0.1 and bulk diffusivity = 10^{-12} cm^2 s^{-1}.
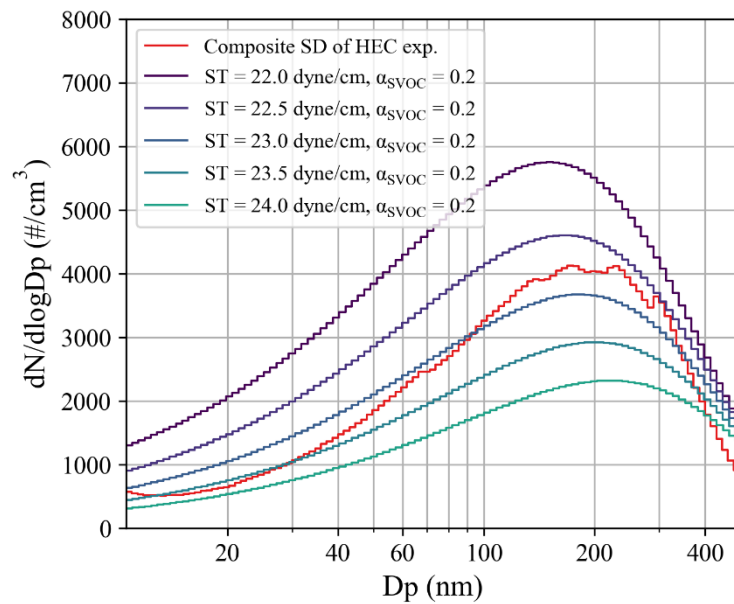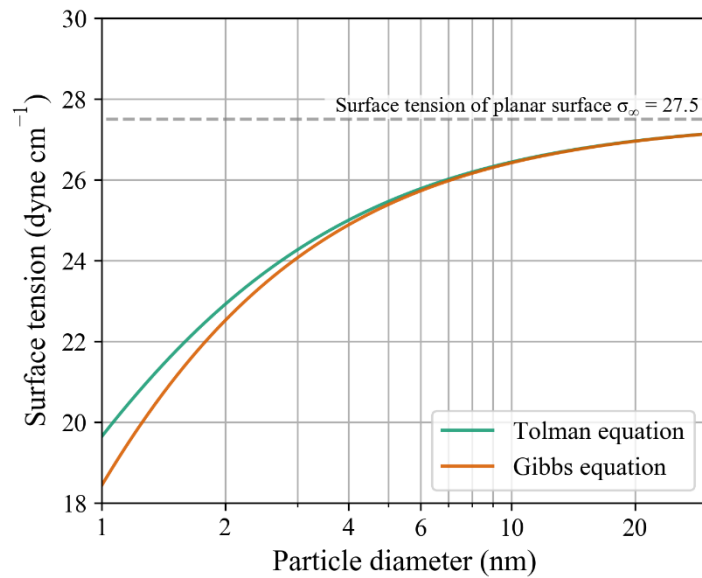

Fig. 14 The steady-state size distribution of simulation with different CNT surface tension incorporated with the composite size distribution of HEC experiments. Parameters: α_{SVOC} = 0.2 and bulk diffusivity = 10^{-12} cm^2 s^{-1}.
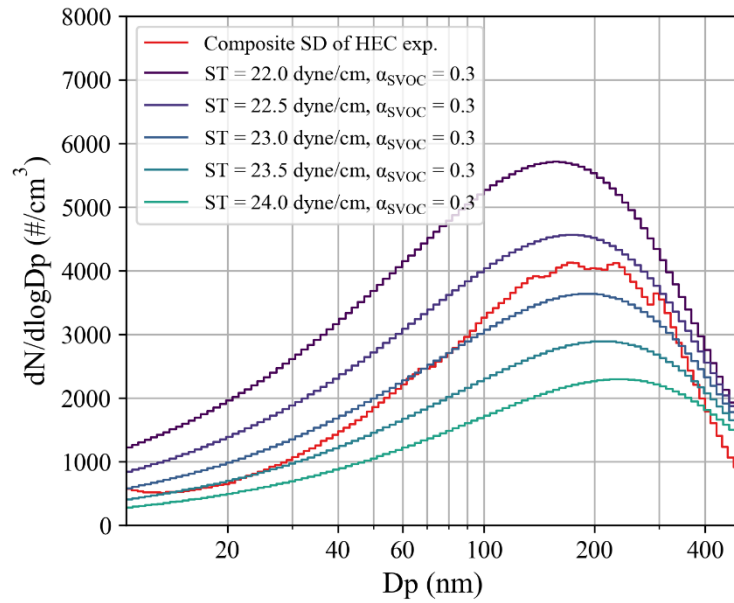
Fig. 15 The steady-state size distribution of simulation with different CNT surface tension incorporated with the composite size distribution of HEC experiments. Parameters: α_{SVOC} = 0.3 and bulk diffusivity = 10^{-12} cm^2 s^{-1}.
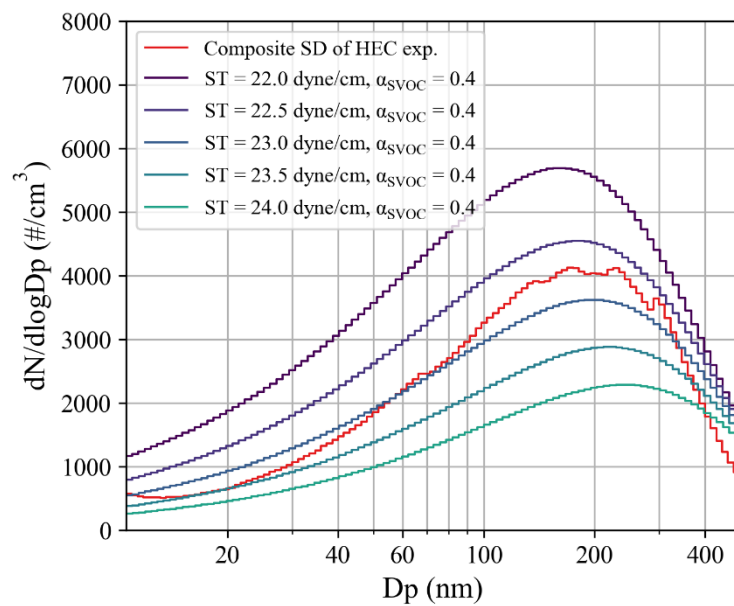
Fig. 16 The steady-state size distribution of simulation with different CNT surface tension incorporated with the composite size distribution of HEC experiments. Parameters: α_{SVOC} = 0.4 and bulk diffusivity = 10^{-12} cm^2 s^{-1}.

Fig. 17 The steady-state size distribution of simulation with different CNT surface tension incorporated with the composite size distribution of HEC experiments. Parameters: α_{SVOC} = 0.5 and bulk diffusivity = 10^{-12} cm^2 s^{-1}.

Fig. 18 Surface tension as a function of particle diameter by considering Tolman surface tension correction with two equations. The surface tension of the planar surface and Tolman length were assumed to be 27.5 dyne cm^{-1} measured in the experiment (Hritz et al., 2016) and 0.1 nm respectively.

51
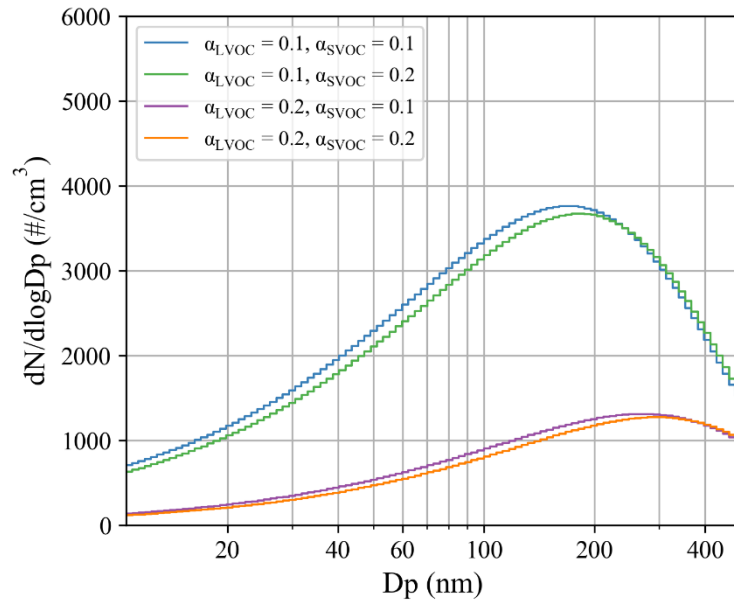
Fig. 19 The Steady-state size distribution of simulation with different accommodation coefficient sets. Parameters: surface tension of CNT nucleation = 23.0 dyne cm^{-1} and bulk diffusivity = 10^{-12} cm^2 s^{-1}.
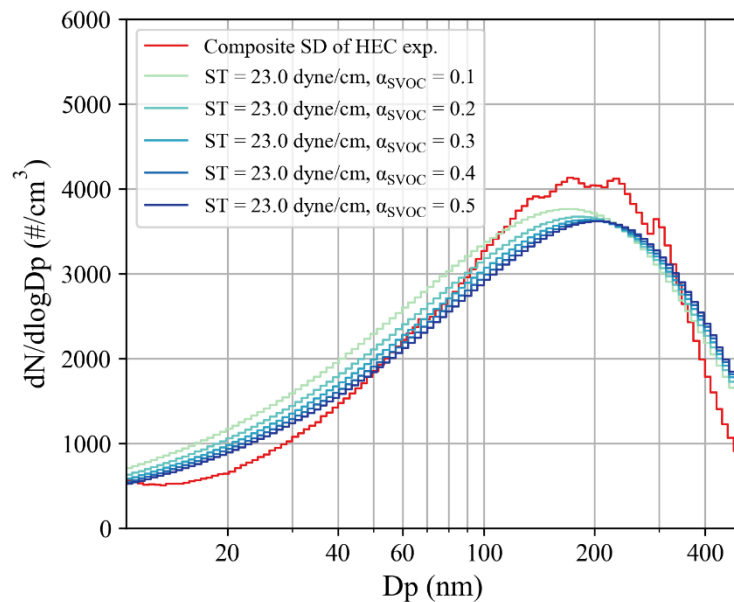
Fig. 20 The steady-state size distribution of simulation with different SVOC accommodation coefficients incorporated with that of HEC experiments. Parameters: α_{LVOC} = 0.1 and bulk diffusivity = 10^{-12} cm^2 s^{-1}.

Fig. 21 The Steady-state size distribution of simulation with different bulk diffusivity. Parameters: surface tension of CNT nucleation = 23.0 dyne cm^{-1}, α_{LVOC} = 0.1, and α_{SVOC} = 0.3.
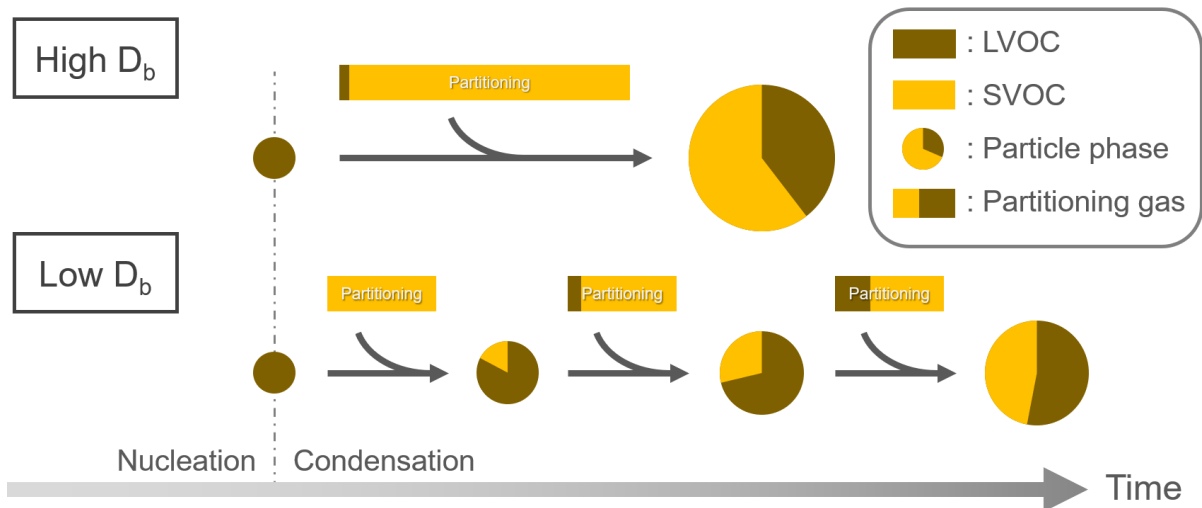
Fig. 22 A brief illustration of vapor partitioning into single particle with different bulk diffusivity D_b ($10^{-6} \geq D_b \geq 10^{-14}$ cm^2 s^{-1}) alone with time. The size of the circle represents the particle size while the length of the bar indicates the amounts of products partitioning into a particle. The ratio does not represent the exact value in simulation but for reference only.
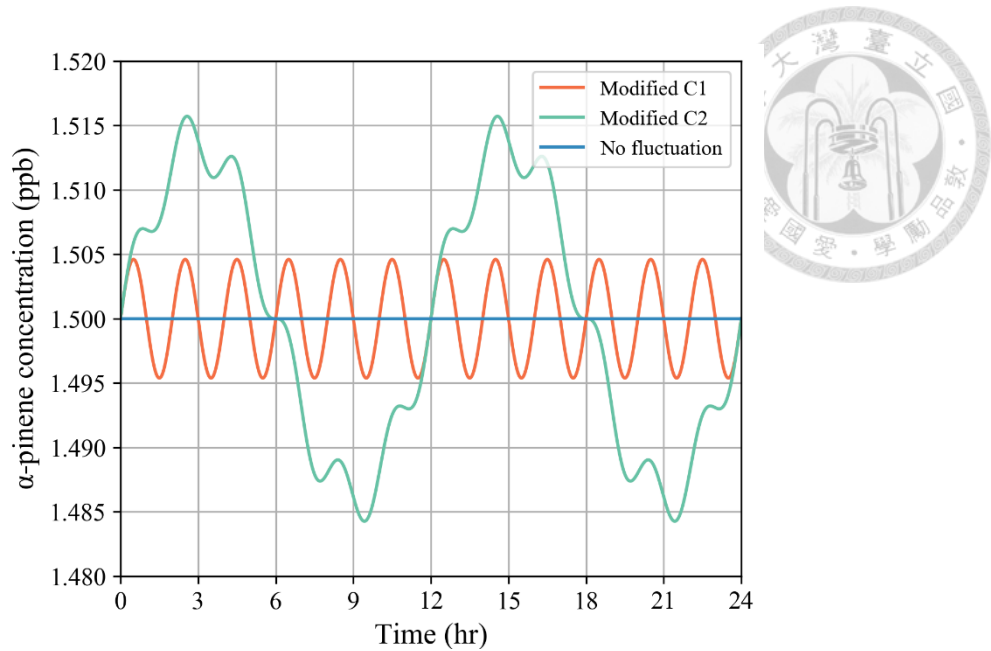
Fig. 23 The fluctuation of α-pinene concentration with the applied function of Eq. 22 for C1 and Eq. 23 for C2 modification.
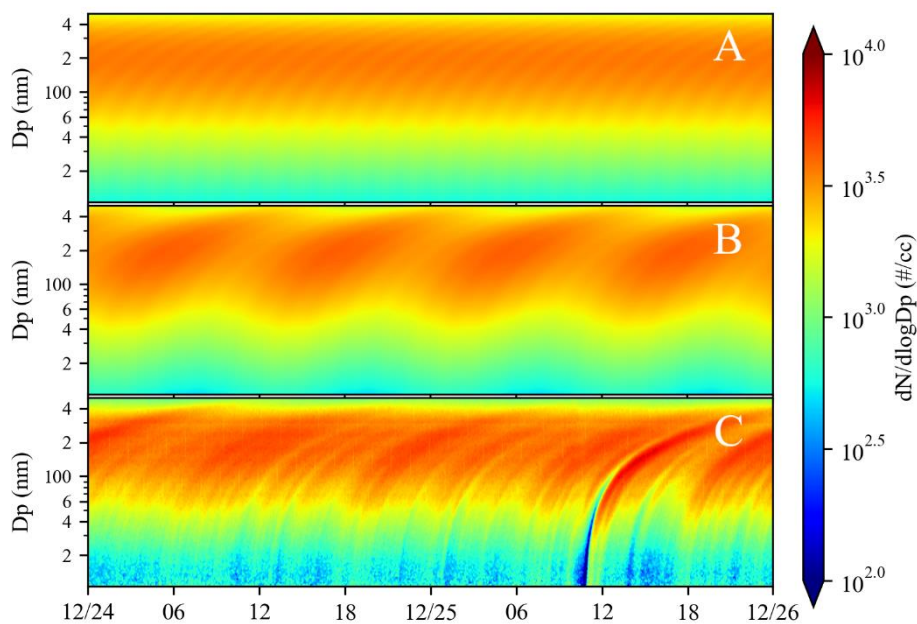
Fig. 24 The influence of α-pinene fluctuational concentration on the simulated particle size distribution ((A) for C1 and (B) for C2 modification) as compared with the observation (2017/12/24 00:00 to 2017/12/26 00:00). Simulation parameters: surface tension of CNT nucleation = 23.0 dyne cm^{-1}, α_{LVOC} = 0.1, α_{SVOC} = 0.3, and bulk diffusivity = 10^{-12} cm^2 s^{-1}.
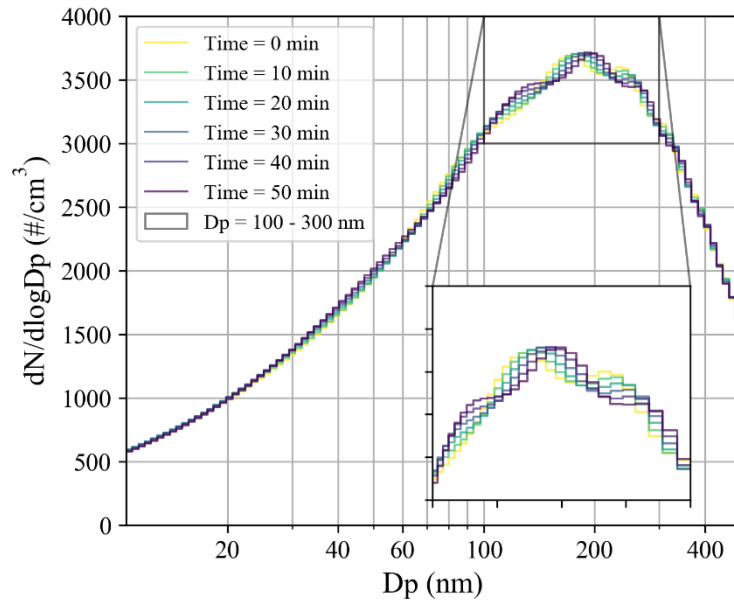
Fig. 25 The simulated size distribution with the C1 setting for selected frame shots around the dynamic equilibrium.
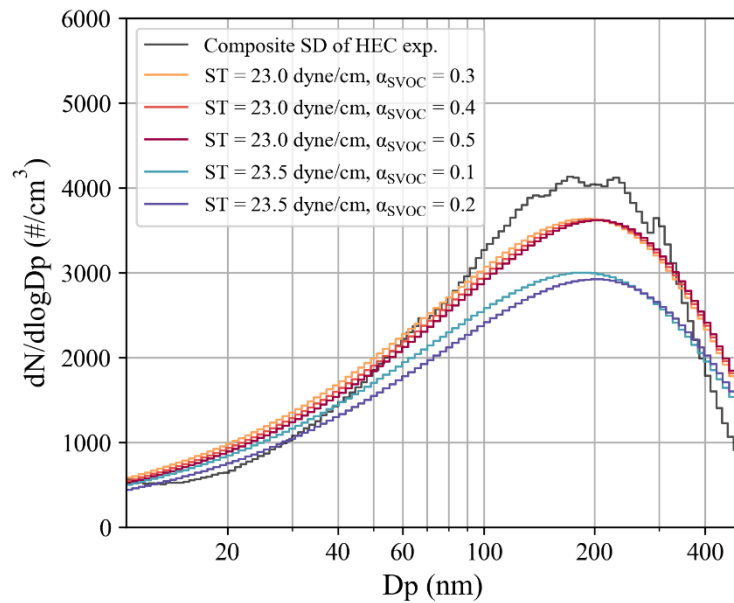

Fig. 26 The steady-state size distribution of simulation with the top five MRE incorporated with that of HEC experiments. Parameters: $\alpha_{LVOC} = 0.1$ and bulk diffusivity $= 10^{-12}$ cm^2 s^{-1}.
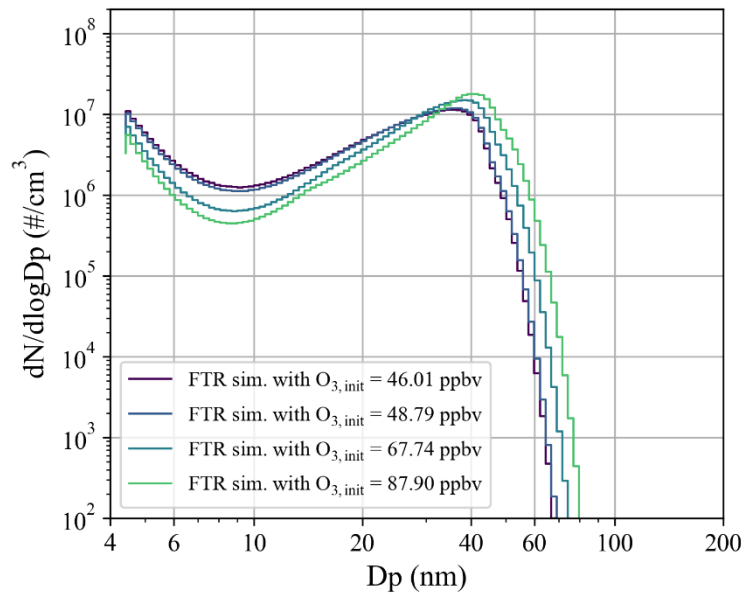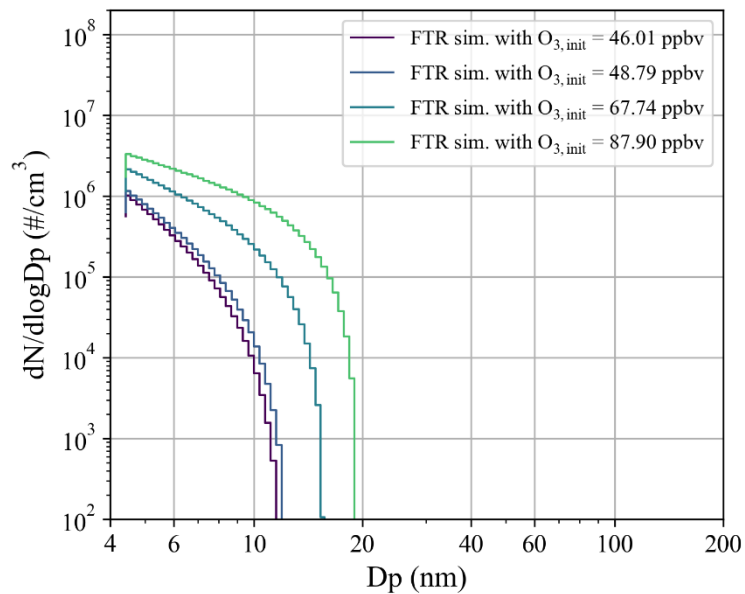
Fig. 27 The size distribution of FTR simulation with different initial ozone concentration. Simulation parameters: surface tension of CNT nucleation = 23.0 dyne cm^{-1}, α_{LVOC} = 0.1, α_{SVOC} = 0.3, bulk diffusivity = 10^{-12} cm^2 s^{-1}, and initial α-pinene concentration = 19.3 ppmv.

Fig. 28 The size distribution of FTR simulation with different initial ozone concentration. Simulation parameters: surface tension of CNT nucleation = 23.0 dyne cm^{-1}, α_{LVOC} = 0.1, α_{SVOC} = 0.3, bulk diffusivity = 10^{-12} cm^2 s^{-1}, and initial α-pinene concentration = 772 ppbv.
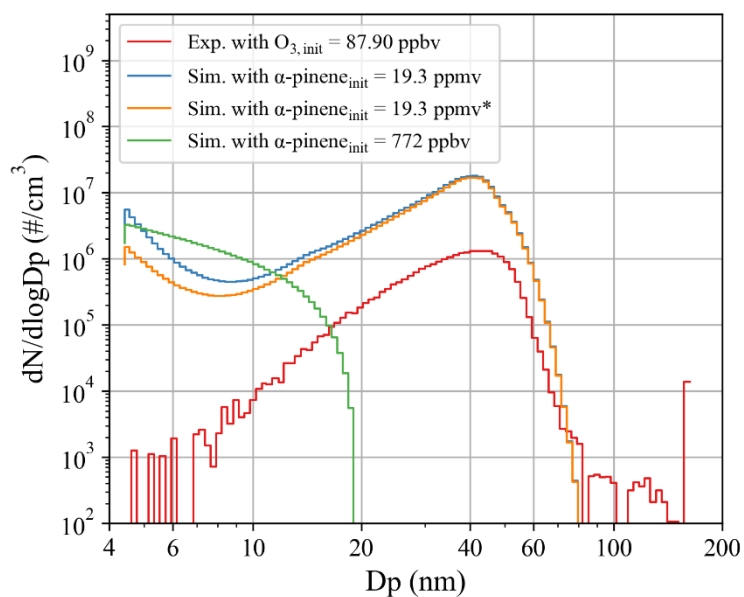
Fig. 29 The size distribution of FTR experiment and simulation with the same initial ozone concentration 87.90 ppbv while initial α-pinene concentrations of simulations were 19.3 ppmv and 772 ppbv respectively. The result marked with * had corrected with 12 s WLC between diffusion dryer and SMPS.
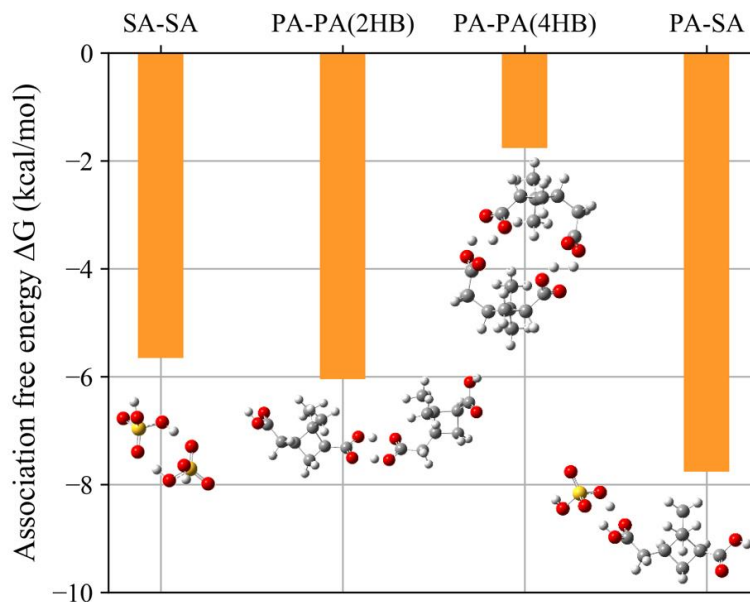

Fig. 30 Association free energy of different molecular pairs: $H_2SO_4 – H_2SO_4$ (SA-SA), pinic acid – pinic acid (PA-PA with 2 hydrogen bonds), pinic acid – pinic acid (PA-PA with 4 hydrogen bonds), and pinic acid – H_2SO_4 (PA-SA). The values were calculated in PW91PW91 / 6-311++G(3df,3pd) level with Gassian09.